Natural Resources Canada | Ressources naturelles Canada

GEOLOGICAL SURVEY OF CANADA
OPEN FILE 9181

Physicochemical limnology of lakes in the Rankin Inlet area of Nunavut

B. Faucher, A.-M. LeBlanc, N. Benoit, É. Girard, and O. Pedchenko

2024

Canada

GEOLOGICAL SURVEY OF CANADA
OPEN FILE 9181

Physicochemical limnology of lakes in the Rankin Inlet area of Nunavut

B. Faucher, A.-M. LeBlanc, N. Benoit, É. Girard, and O. Pedchenko

2024

Recommended citation
Faucher, B., LeBlanc, A.-M., Benoit, N., Girard, É., and Pedchenko, O., 2024. Physicochemical limnology of lakes in the Rankin Inlet area of Nunavut; Geological Survey of Canada, Open File 9181, 41 p. https://doi.org/10.4095/p4bwndvvbb

Publications in this series have not been edited; they are released as submitted by the author.

ISSN 2816-7155
ISBN 978-0-660-72594-9
Catalogue No. M183-2/9181E-PDF
https://doi.org/10.4095/p4bwndvvbb

Physicochemical limnology of lakes in the Rankin Inlet area of Nunavut

Benoit Faucher[1], Anne-Marie LeBlanc[1], Nicolas Benoit[2], Étienne Girard[2], and Oleksandra Pedchenko[2]

[1]Natural Resources Canada (Geological Survey of Canada), 601 Booth Street, Ottawa, Ontario

[2]Natural Resources Canada (Geological Survey of Canada), 490 rue de la Couronne, Québec, Québec

SUMMARY

With the expected increase in mining activities in Canada's Northern regions due to global demands for critical minerals, there is a pressing imperative to devise novel and dependable methods for identifying lakes that may be situated above unfrozen ground sections (i.e., taliks) in continuous permafrost environments. When taliks fully penetrate the permafrost, they may enable interactions between surface and subpermafrost groundwater, presenting significant challenges for mining operations. This report provides detailed baseline data on water temperature, conductivity, and sometimes pH measurements made via an unmanned air vehicle for lakes near Rankin Inlet, Nunavut, made in April and September 2023. This dataset will feed our thermal and geophysical models for talik identification and conceptual cryo-hydrogeological models for simulating subsurface hydrogeological flow in continuous permafrost regions. Notably, our findings reveal that in April, water column temperatures within our selected lentic basins ranged from 0.1 to 2 °C directly below the ice cover and from 1.7 to 3.5 °C at the water-sediment interface. Conversely, in September, the water column of the surveyed basins was isothermal. These temperature profiles suggest that the surveyed lakes exhibit characteristics indicative of cold polymictic basins, with winter stratification being more pronounced with increasing basin depth. Additionally, our conductivity measurements indicate a salinity-density relationship within the lakes' water column. Specifically, measurements directly beneath the ice cover and near the lake-bottom ranged from 74 to 168 µS cm^{-1} and 77 to 352 µS cm^{-1} in April 2023, respectively, while surface and lake-bottom conductivities ranged from 44 to 111 µS cm^{-1} and 73 to 488 µS cm^{-1}, respectively, in September. Moreover, preliminary evaluations of cryoconcentration effects on solute loading during ice-on and ice-off seasons indicate a potential contribution to the observed discrepancies in water column conductivities between the two field sampling seasons. However, conducting additional geochemical analyses is crucial to validate this hypothesis and explore the possibility of other natural phenomena that might account for these differences.

INTRODUCTION

Arctic and Subarctic lentic water bodies serve as crucial indicators of climate change, as their physical, chemical, and biological properties respond swiftly to rapid environmental shifts (Goldman et al., 2012). These stand out from their temperate counterparts through several distinctive features. These distinctions arise namely from differences in their origin (e.g., thermokarst-derived, or glacial-derived), from their characteristic short ice-free seasons and long ice-covered periods (and associated impacts on nutrient cycling, light penetration, water column mixing, and gas exchanges), and most notably because they are often situated in areas underlain by perennially cryotic ground (i.e., permafrost) (Muster et al., 2017). In areas where permafrost is continuously present (i.e., continuous permafrost), interactions between surface water bodies (including near-surface groundwater) and subpermafrost groundwater are limited. This water

movement restriction is due to the quasi-impermeability of permafrost, effectively serving as an aquitard that hinders water movement between surface waters and deep groundwater (van Everdingen, 1990; Yang & Kane, 2020). Nonetheless, surface-subsurface groundwater interactions may occur within unfrozen sections of the ground (i.e., taliks) below large and deep lakes (~> 2 m depth) that may penetrate the permafrost completely (Mackay, 1963). Those unfrozen ground sections, known as "sublacustrine open taliks" may present a considerable challenge for mining operations in permafrost landscapes, especially when these operations intersect with these taliks (Golder, 2021; LeBlanc et al., 2022). This adds a layer of complexity to underground mineral extraction activities in the Arctic. For example, the operational timeline of mining activities could be significantly curtailed when faced with challenges in effectively managing the influx of (potentially saline) groundwater into a mine intersecting a sublacustrine open talik. Consequently, given the anticipated surge in mining operations in Canada's North driven by global demands for critical minerals (Maloney, 2021), there is a pressing imperative to develop new and reliable techniques for identifying lakes potentially underlain by open taliks. Additionally, there is a need to enhance our understanding of the hydrological connections between these sublacustrine open taliks and the subpermafrost groundwater.

This report provides comprehensive baseline data on the water column temperature and conductivity (and, in some instances, pH) of several lakes near the hamlet of Rankin Inlet, Nunavut, an area in the Kivalliq region that is currently experiencing a renewed interest in development activities. The observations cover the ice-free season (September 2023) and the ice-covered season (April 2023). These parameters are crucial in evaluating the surface water basins' thermal regimes and mixing patterns. The gathered data will feed the thermal and geophysical models for talik identification, and the conceptual coupled cryo-hydrogeological systems models we are currently developing for simulating subsurface hydrogeological flow within continuous permafrost landscapes as part of our multidisciplinary research project. This modelling is particularly relevant for simulating the presence of sublacustrine open taliks.

STUDY AREA

Geology

Rankin Inlet is situated on the western coast of Hudson Bay in the Kivalliq region of Nunavut (Canada) (Fig. 1A) within the western Churchill Province of the Canadian Shield. Its complex geology consists of Archaean Rankin Inlet Greenstone Belt felsic volcanic rocks intercalated with mafic volcanic and sedimentary rocks and granodioritic to tonalitic intrusions (Lawley et al., 2016). Glacial, marine, and glaciofluvial deposits, including eskers, with numerous bedrock outcrops, comprise most of the surficial geological units (McMartin, 2002). Those shape the area with elevations ranging from sea level to approximately 150 m above sea level within the vicinity of our surveyed lakes. During the Wisconsin Glaciation, the Laurentide Ice Sheet covered the region and receded by ~6 kyr BP (Dyke, 2004). The postglacial Tyrrell Sea extended up to 150 km inland from the current coastline over the isostatically depressed land surface, reaching a maximum elevation of approximately 170 m above the present sea level (Dyke, 2004; McMartin et al., 2023; Randour et al., 2016).

Climate

Between 1981 and 2020, the mean annual air temperature (MAAT) for Rankin Inlet was −10.3 °C, with an average increase of 0.05 °C/year (ECCC, 2023) (Fig 2). The average total precipitation

over the same period was 315 mm, with rainfall accounting for 184 mm and snow precipitations contributing 131 cm. There was no significant trend in total precipitation during the 1981 to 2020 period. The warmest year in the historical record for Rankin Inlet was 2010, which was followed by a cooling period consistent with the observed anomaly over the eastern Canadian Arctic region (Bell & Brown, 2018).

Permafrost

Continuous permafrost is pervasively present in the Rankin Inlet area. Its base is estimated to be between 285 m and 430 m below the surface, with the thinnest sections of the perennially cryotic ground being near lakes (Golder, 2021). The geothermal gradients were estimated to be between 0.012 and 0.018 °C/m (Golder, 2014), while the mean annual ground temperature at the top of permafrost ranges between –9.5 and –5.5 °C. Active-layer thickness ranges from ~0.5 m in organic-rich alluvial-marine sediments to ~1.6 m in marine and organic-poor till deposits (LeBlanc & Oldenborger, 2021).

Water Bodies

In contrast to rarely observed thermokarst lakes, kettle lakes and lakes shaped by glaciofluvial, or glacial processes are common in the area (Golder, 2014). Those are typically seasonally ice-covered from early October to June (Golder, 2014). Their preferential orientation of the area's lakes (northwest-southeast) follows the orientation of glacial and glaciofluvial deposits. The surface area of the lentic water bodies ranges from 200 to 180 x 10^6 m² (Peter Lake) with an average and median of 71,000 and 5,400 m², respectively. Maximum depths of about 100 surveyed lentic basins ranged from 0.11 to 23.5 m (Golder, 2012a, 2012b). Lake expansion and drainage were attributed to thermokarst processes, observed in fine-grained and ice-rich sediments, and thickening of the active layer likely caused by the increase in subsurface water storage in coarse-grained and ice-poor sediments, respectively (LeBlanc et al., 2020).

METHODS

Spring 2023 (April) water column profiles

The positioning of the on-ice water column profile surveys (n=12; see Table A1 and Fig. 1) aligns with time-domain electromagnetic (TEM) soundings carried out in April 2023 for talik investigations (Oldenborger, 2024). During this period, an ice auger was employed to penetrate the ice cover at floating ice locations (Sladen et al., 2024), with subsequent ice thickness and lake depth measurements conducted using a weighted line.

Water temperature and specific conductance (conductivity) alone (no pH measurements during that field season) were gauged using a freshwater conductivity data logger (*Onset HOBO U24*,), boasting a resolution of 0.01 °C and 1 µS cm^{-1}, and an accuracy of 0.1 °C and 5 µS cm^{-1}. The probe was calibrated in the laboratory using a 1413 µS cm^{-1} solution. The results showed that the logger readings were approximately 2 % lower than the calibrated solution.

Initially affixed to the weighted line at 0.45 m (sites 1 and 18), and later at 1 m (sites 2, 11 to 16, 19, and 20) from the line bottom, unless the lake's shallowness dictated otherwise (Sites 3 and 8 at 0.22 and 0.10 m from the bottom, respectively), the logger was slowly lowered to prevent sediment disturbance at the lake-bottom (Fig. 3). Measurements were taken incrementally (reading interval was set at 10 seconds) from the lakes near bottom to their surface at intervals of 1.85 m, with the

logger stationed at each depth for approximately 3 to 5 minutes, except for sites with shallow waters (sites 3, 8, and 11), where it remained stationary for 8 to 10 minutes at the lowest possible lake depth.

Summer 2023 (September) water column profiles

In fall 2023 (September), water column profiles (n=14; see Table A1 and Fig. 1B) were conducted at some of the April 2023 TEM sites (excluding sites 1, 3, 8, 13 & 16) and additional ones (sites 1A, 10, 6, 9, 12A, 17, & 21).

Water column surveys were undertaken remotely from the lakeshore using a *DJI Matrice 300 RTK* Unmanned Aerial Vehicle (UAV) to which two probes (pre-programmed to take readings every 2 seconds) were attached to a 25 m long 4 mm thick Kevlar rope (Fig. 4). The first probe employed was a *Solinst 5 LTC Levelogger* with accuracy and resolution specifications for its level, temperature, and conductivity readings: 5 cm, 0.05 °C, and 5 µS cm^{-1}, and 0.001 % FS, 0.003 ºC, and 0.1 µS cm^{-1}, respectively. This probe was calibrated in the laboratory using a 1413 µS cm^{-1} solution. The results showed that the logger readings were approximately 2-3 % lower than the calibrated solution. Additionally, a *HOBO MX2501* served as the second probe, measuring water column pH and temperature with an accuracy and resolution of 0.10 pH units, 0.2 °C, and 0.01 pH units, and 0.024 °C, respectively. This probe underwent calibration in the laboratory using solutions with pH values of 4.01, 7.01, and 10.01. The results showed that the logger readings were approximately ±1 to 2 % around the calibrated solution.

Once safe flying conditions (i.e., good weather and visibility) were confirmed, the pilot initiated the planned flights of the UAV for each site of interest. Automating flight plans facilitated our ability to return to the same sites for further measurements, ensuring consistency and comparability in data collection. Upon the UAV's arrival at the site of interest, the pilot manually controlled the UAV to lower the probes to a depth of approximately 1 meter in the water column of the basin. The UAV then remained stationary for at least 30 seconds, allowing the probes to acclimate to the water. Following this, depending on the maximum depth of the surveyed sites, the drone gradually lowered the probes in approximately 2-meter increments. It paused for at least 30 seconds at each depth plateau until reaching the interface between the water and sediment. This approach ensured that measurements were taken systematically from the top down, providing a comprehensive understanding of the water column's temperature, pH and conductivity.

RESULTS

Little Meliadine Lake

Site 1

During the ice-on survey conducted in April at site 1, situated in the central portion of Little Meliadine Lake's (LML) western section, the depth profile revealed a linear increase in water column temperatures beneath the approximately 1.7 m thick ice cover. The temperatures ranged from 0.9 °C at a depth of 3.51 m to 2.3 °C at a depth of 9.00 m (Fig. 5). Additionally, conductivities remained relatively consistent with depth, showing a slight increase, and varying within the range of 73 to 76 µS cm^{-1} (i.e., within the logger accuracy of 5 µS cm^{-1}).

Site 1A
At Site 1A, located approximately 500 m southeast of Site 1, the September survey exhibited a gradual linear temperature increase with depth within the water column. Temperatures rose marginally from 8.3 °C at a depth of 2.00 m to 8.9 °C at 8.50 m depth, corresponding to the site's lake bottom (Fig. 6). In terms of conductivities, the water column demonstrated stability, maintaining values around 63 µS cm^{-1} between depths of 2.00 and 6.00 m, but notably increased to 97 µS cm^{-1} at the water-sediment interface. Additionally, pH values of the water exhibited an upward trend, ascending from 6.7 at 2.00 m depth to 7.2 at 6.00 m depth, before showing a decline towards lower values at the site's lake-bottom, with a pH of approximately 6.8.

Site 2
Beneath the ~1.8 m thick ice cover in April, water column temperatures in the deepest section of LML's east portion increased from 0.4 to 2.0 °C between 2.60 and 11.75 m, with the latter measurement taken approximately 1.00 m above the site's lake-bottom (Fig. 7). In September, the water column temperatures from 1.00 m below the surface to the site's lake-bottom exhibited a decrease from 10.1 to 7.5 °C. Conductivity values in the water column during the April survey remained consistent with depth, staying within the 76 to 81 µS cm^{-1} range. In September, these values were lower than in April and showed an increase in depth, ranging from 44 to 73 µS cm^{-1} between 1.00 m below the surface and the site's lake bottom. In September, pH values of the water column experienced a slight rise from 7.3 to 7.5 between depths of 1.00 and 11.00 m, followed by a decrease to 6.7 at the site's lake bottom.

Site 3
Site 3 was LML's easternmost survey site. In April, water temperatures and conductivities directly below the ~1.5 m thick ice cover (~0.40 m above the site's lake-bottom) were measured at 0.2 °C and 85 µS $cm^{-1,}$ respectively (Fig. 8).

Site 18
The deepest physicochemical water column survey at LML was undertaken in its north easternmost section (site 18). In April, water temperatures displayed an exponential-like increase, rising from 1.0 below the ~1.85 m thick lake ice to 2.8 °C at a depth of 16.80 m (Fig. 9). In contrast, during the September field campaign, the lake's temperature exhibited a decline from 9.5 to 8.7 °C between depths of 2.50 and 17.30 m (the latter depth being the site's lake-bottom). Conductivity values demonstrated consistency, indicating stable values within the 73-92 µS cm^{-1} and 62-63 µS cm^{-1} ranges for April and September. However, conductivity values substantially increased at the site's lake bottom, reaching values of 194 and 154 µS cm^{-1}, in April and September, respectively. The pH of the water column exhibited an increasing trend with depth in April, starting at 6.4 (at 2.50 m) and reaching a maximum of 7.1 at 15.97 m before gradually decreasing to 6.8 at the site's lake-bottom.

Site 19
In April, beneath the ~1.8 m thick ice cover at the south westernmost site on Little Meliadine Lake (site 19), water temperature exhibited a linear increase with depth, ranging from 0.5 °C at 2.31 m to 2.7 °C at 6.07 m (Fig. 10). Conversely, during the ice-off period in September, a slight linear decline in water column temperatures was observed, shifting from 8.8 to 8.4 between depths of

1.00 and 7.10 m, reaching the site's lake-bottom. Like the observed linear increase in water temperatures in April, conductivity readings during that same field season displayed a linear increase, ranging from 78 to 92 µS cm^{-1} between depths of 2.31 and 6.07 m. In contrast, conductivity values in the water column in September remained stable with depth (64 µS cm^{-1}) up to the site's lake-bottom, where they increased to 75 µS cm^{-1}. In September, the pH of the water column demonstrated an increasing trend with depth, starting at 6.7 (at 1.00 m) and reaching a maximum of 7.1 at 5.34 m before gradually decreasing to 6.7 at the site's lake-bottom.

First Landing Lake

Site 10

In September, shallow waters in the northernmost section of First Landing Lake (FLL; site 10) had a temperature and conductivity of 8.2 °C and 97 µS cm^{-1}, respectively (Fig. 11). Further, the pH at the water/sediment interface was 7.2.

Site 11

Site 11 on FLL was situated ~200 m south of site 10. A water temperature of 0.5 °C was measured at a depth of 2.12 m in April (below the ~1.8 m thick ice cover; Fig. 12). Conversely, lake-bottom waters at that site (3.60 m depth) in September were measured at 7.7 °C. The water column at 2.12 m (April) and 3.60 m (September) had conductivity values of 151 and 110 µS cm^{-1}, respectively. Finally, site 11's bottom waters had a pH of 7.3 in September.

Site 12

In April, beneath the ~1.7 m thick ice cover, the temperature of the water column at site 12 increased with depth from 0.1 °C at 2.44 m to 3.7 °C at 15.60 m below the surface, with notable increases observed particularly in the upper and bottom portions of the water column (Fig. 13). Conversely, in September, water temperatures increased from 6.9 °C at 0.80 m to 7.6 °C at the site's lake-bottom (16.30 m). A slight increase in conductivity values for the water column below the ice cover in April was noted for depths between 2.44 and 13.72 m (from 141 to 173 µS cm^{-1}). This was followed by a sharp increase at the bottom of the site's water column (249 µS cm^{-1}). Contrarily, conductivities in September remained very stable with depth (~111 µS cm^{-1}). Further, pH values in September increased with depth from 6.7 (0.8 m) to 7.6 (16.3 m; site's lake-bottom).

Site 13

In April, the temperature of the water column below the ~1.8 thick ice cover in the westernmost section of FLL (site 13) increased from 0.1 to 1.7 °C between depths of 2.01 and 5.67 m (the latter measurement having been done ~1.00 m above site 13's bottom) (Fig. 14). At that same date, conductivities were stable with depth and remained in the 145-148 µS cm^{-1} range.

Second Landing Lake

Site 15

Below the ~1.7 m thick ice cover, in April, temperatures in Second Landing Lake's (SLL) water column at site 15 increased from 2.1 to 2.9 °C between 1.94 and 5.70 m (Fig. 15). In September, the water temperature at the site's lake-bottom (7.20 m) was measured at 7.6 °C. Conductivity

values slightly increased with depth in April (shift from 168 to 179 µS cm^{-1} between depths of 1.94 and 5.70 m). In comparison, in September, the site's lake-bottom water had a conductivity and pH of 97 µS cm^{-1} and 7.1.

Site 16

In the central portion of SLL (site 16), in April, the temperature of the water column below the ~1.8 m thick ice cover increased from 1.3 to 1.9 °C between our two measuring depths of 1.96 and 3.84 m (Fig. 16). The conductivity of the water also slightly increased between the aforementioned depths (from 162 to 170 µS cm^{-1}).

Site 17

In September, the temperature of the water column at a depth of 1.70 m was measured at 7.8 °C (Fig. 17). Further, the conductivity and pH of the water at that depth were 79 µS cm^{-1} and 7.5, respectively.

Lake A

Site 8

In April, in the central portion of Lake A (site 8), the temperature of the water column at a depth of 1.69 m (below the ~1.6 m ice cover and right above the site's lake-bottom situated at ~1.80 m) was measured to be ~0.1 °C (Fig. 18). The conductivity of waters at that depth was measured at 352 µS cm^{-1}.

Lake B

Site 6

In September, in the central portion of Lake B, the site's bottom waters' temperature, conductivity, and pH were measured at 7.0 °C, 227 µS cm^{-1} and 6.7, respectively (Fig. 19).

Lake C

Site 20

In April, the waters at a depth of 2.08 m, below the ~1.8 thick ice cover in the central portion of Lake C (site 20), registered a temperature of 1.1 °C (Fig. 20). In September, water temperatures exhibited an increase from 7.8 to 8.3 °C between depths of 0.10 and 3.13 m. During the April survey, the conductivity of the waters at the 2.08 m depth point was measured at 289 µS cm^{-1}. In September, measurements between 0.10 and 3.13 m depths indicated that conductivity values increased with depth, ranging from 93 to 111 µS cm^{-1}. Additionally, pH values showed a corresponding trend, decreasing from 7.6 to 6.8 with increasing depth during the September measurements.

Lake D

Site 9
In September 2023, bottom waters (depth of 1.40 m) in the central portion of Lake D (site 9) had temperature, conductivity, and pH values of 8.0 °C, 220 µS cm^{-1} and 6.9, respectively (Fig. 21).

Lake E

Site 21
The bottom waters (~1.2 m) in the central portion of Lake E (site 21), in September 2023, had a temperature, conductivity, and pH of 8.6 °C, 488 µS cm^{-1} and 8.1, respectively (Fig. 22).

DISCUSSION

Thermal stratification and mixing dynamics

The primary influencers of thermal stratification in freshwater surface basins are the disparities in water column temperatures. It is crucial to understand the mixing dynamics that contribute to the stratification of freshwater lentic basins, as this knowledge plays a pivotal role in determining whether these basins exhibit seasonal or perennial thermal stratification or are predominantly mixed to the bottom (Kirillin & Shatwell, 2016). Such stratification's implications significantly affect various biological and chemical processes within the water column (Boehrer & Schultze, 2008; Boyce, 1974).

During our measurements in the spring of 2023, water column temperatures in the surveyed lakes displayed a non-isothermal, stratified pattern. The waters directly beneath the 1.6 to 1.8 m ice covers ranged from approximately 0.1-2 °C. However, it is important to understand that the water column temperature readings directly below the ice cover at sites having very shallow residual water columns might be slightly higher than what's indicated in our data. Indeed, it's possible that conduction cooling, resulting from interactions between the shallow residual water column and the cold air at the time of our surveys, compounded by the low residual water volume at those sites, may have caused the water temperature to be lower than its actual temperature under the ice. Nonetheless, in April, water temperatures increased to around 1.7-3.5 °C near the bottom, approximately 1 m above the water/sediment interface. This stratification is typical for freshwater lakes that undergo the development of a seasonal ice cover. As colder air temperatures set in during the fall, surface waters, cooling to around 4 °C (the temperature at which water is the densest), sink to the lake-bottom. In contrast, cooler and more buoyant waters remain at (or near) the surface until they reach freezing at or near 0 °C. The overlying ice cover then maintains temperatures slightly below 0 °C directly beneath it, ensuring that these colder waters remain afloat on top of the denser and warmer bottom waters (Boehrer & Schultze, 2008). Therefore, it is evident that density differences driven by water temperature were the primary factors responsible for the stratification observed in the spring water columns of the lakes under investigation. Furthermore, our under-ice water column temperature measurements in April 2023 suggest that the intensity of stratification patterns within the surveyed basins is linked to their depth (Fig. 23). Specifically, the deepest basins exhibited significant temperature increases, indicating a depth-density relationship, with measurements near the lake-bottom reaching approximately 4 °C compared to shallower lakes having lower temperatures at or near the water-sediment interface.

During late summer in September 2023, water column temperatures in our surveyed lakes exhibited quasi-homogeneity, characterized by near-isothermal conditions with depth. Near-surface water temperatures ranged from approximately 7-10 °C, while bottom waters maintained temperatures between about 7 and 9 °C. These water column temperatures aligned well with the local maximum air temperatures recorded during our late summer sampling period, ranging from 6.9 to 10.1 °C (ECCC, 2023). Similar temperature patterns than those we measured in September 2023 were observed during the July-August 2011 survey of other nearby lakes and ponds located on the periphery of the Agnico Eagle Meliadine Mine, situated approximately 25 km NNW of Rankin Inlet and about 10 km NNE of Little Meliadine Lake (Golder, 2012b). During the 2011 survey, these lakes' surface and bottom water temperatures were nearly identical, fluctuating between 14.2 and 19.1 °C, with surface-bottom temperature differences ranging from 0.0 to 0.5 °C (Table A2). These observations correlated well with the maximum recorded air temperatures in Rankin Inlet during the 2011 summer lake water depth profiling campaign (ECCC, 2023). Both sets of measurements are consistent with the lake-type classification established by (Lewis, 1983) (Fig. 24), suggesting that shallow lentic basins at latitudes around 62.8 °N are likely to be of the cold polymictic type. However, since depth profile measurements were conducted only once during the summer for each basin in 2023 and 2011, it remains to be confirmed whether the water column completely mixes on a discontinuous (weekly) or continuous (daily) basis during the ice-off period, despite Lewis' (1983) classification favouring the latter as more probable. Nevertheless, the depth profiling measurements in 2023 and 2011 for the shallow surveyed lakes and ponds indicate isothermal water columns and the absence of a hypolimnion (dense bottommost layer) during the summer (with no significant correlation between lake bottom temperature and depth; Fig. 23) and likely throughout most of the ice-free period.

This underscores the highly efficient wind-driven mixing of shallow lakes in Tundra environments (Brewer, 1958; Mackay, 1963), where there are no obstacles such as forests to dampen gusts. The efficient mixing, combined with sensible air-water heat exchanges through conduction at the lake-atmosphere interface, plays a crucial role in preserving isothermal conditions in the water column of our surveyed lakes during the ice-off period. This balance with atmospheric conditions (e.g., Boehrer & Schultze, 2008) guarantees that our surveyed lakes uphold uniform temperatures across their entire water columns during most of the ice-free season.

Seasonal variations in conductivities with depth

The concentration and nature of dissolved ions in the water column of freshwater Arctic surface basins, are influenced by various surface and subsurface processes and features. These include factors such as permafrost, bedrock, surficial deposits, vegetation, hydrology, evaporation, oceanic proximity, and marine legacy effects (Klanten et al., 2021). Here, we leveraged our conductivity measurements, recorded in micro siemens per centimetre ($\mu S\ cm^{-1}$), within our targeted water bodies in April and September 2023 to deduce their total dissolved solids (TDS) loading (e.g., Taylor et al., 2018; see Table A1). We aimed to gain insights into variations in TDS loading during distinct ice-on and ice-off periods and use this information to initiate or validate our mass transport modelling results. The conductivity/TDS data are also used for interpreting Time-domain Electromagnetic (TEM) surveys (Oldenborger, 2024).

In September 2023, during the ice-off period, conductivity at the lentic basins' surface and bottom exhibited a range of 44 to 111 $\mu S\ cm^{-1}$ and 73 to 488 $\mu S\ cm^{-1}$, respectively. The highest

conductivities were observed in the water columns of lakes B, D, and E's basins. This result aligns with expectations, as these lakes are the shallowest among the surveyed ones and, therefore, more susceptible to solute evapoconcentration, leading to associated pH increases (Faucher et al., 2022). This explains the highest conductivity and pH values recorded in the shallow waters of lake E's site 21 (488 µS cm-1; pH = 8.1). Conversely, due to the correlation between morphometric basin properties (e.g., surface area, water column depth, and associated volume) and the potential impact of evaporative processes on dissolved solute loads, the lowest water column conductivity values were unsurprisingly measured at sites on LML which is the deepest among our surveyed lakes. Additionally, in basins with multiple depth measurements, the water column conductivity is highest at the water-sediment interface. This is anticipated in quasi-isothermal water columns due to the influence of solute loads on water density – the mass of water increases as more salts are dissolved (Dougherty, 2001). However, our understanding is limited by insufficient geochemical data, namely major ion concentrations, to comprehensively explain whether factors other than dissolved solute-driven density fluctuations within the water column alone may contribute to the TDS load at the bottom. The observed conditions of higher conductivities at the water-sediment interface were within the water columns of lakes suspected of hosting sublacustrine open taliks (i.e., LML and FLL; LeBlanc et al., 2022), where hypersaline subpermafrost groundwater inputs (approximately 1.8 times seawater; Golder, 2012b) might be contributing to the water budget of these basins. Even if these contributions are minimal, they could potentially enhance the density gradients between surface and bottom waters in these basins.

In contrast, earlier in 2023, during the ice-on period in April, conductivity within surveyed lakes fell within the range of 74-168 µS cm^{-1} below the ice covers, and it fluctuated from 77 to 352 µS cm^{-1} at approximately 1.00 m from their bottom. Similar to our observations in September 2023, and for reasons previously discussed, the water column conductivity in April 2023 consistently remained highest near the bottom of their water column, especially for the deepest sites in lakes suspected of hosting sublacustrine open taliks, suggesting that hypersaline subpermafrost groundwater contributions slowly infiltrating the bottom of these basins, even during the spring, could theoretically contribute to higher salinity (and density) in bottom waters. Moreover, conductivity measurements indicated that the water column's salinity in the basins of interest was higher during the ice-on period. While reliable geochemical data is lacking to rule out hypersaline subpermafrost groundwater contributions and other potential processes fully, we propose that the discrepancy between summer and spring water column conductivities could primarily be attributed to the rejection of solutes from the solid phase (i.e., ice) during ice-cover formation and the concentration of these solutes in the residual waters of our studied basins (Killawee et al., 1998). Experiments conducted by Santibáñez et al. (2019) demonstrate that the migration of the freezing front during ice cover formation on seasonally ice-covered lakes predominantly excludes major ions (with degrees of variation depending on the conservative nature of specific ionic species) from the ice phase and gradually accumulating in the remaining liquid waters. This process mirrors the impact of evaporative processes on solute concentration in residual waters. Consequently, by acquiring ample data on major ions (or total dissolved solids loading) and disregarding ionic inputs/outputs from groundwater and nearby catchments, one can estimate the impact of cryoconcentration on the evolution of solute load during ice cover formation using a mass balance method. This process entails dividing the dissolved concentration of major ions during the summer season by the portion of lake volume change during the ice-on period (e.g., Palmer et al., 2019) to gauge the average TDS loading (or conductivity) of the water column throughout the ice-on period.

One of the smallest basins we surveyed during the ice-on and ice-off period is Lake C (i.e., site 20). Even though we do not have bathymetric data for this basin, a glance at satellite imagery and the bottom-fast ice detection work done by Sladen et al. (2024) reveals that it most likely hosts a deep central portion (where we conducted our surveys and measured a maximum depth of ~3.13 m) surrounded by narrower and shallower terraces. For a basic cryoconcentration modelling exercise, if the central and deepest portion predominates in shaping the lake's configuration, we can estimate that Lake C has a lake-wide water column depth of approximately 3 m. During the ice-on period, the formation of an approximately 1.8 m thick ice cover would decrease the residual water column depth to about 1.25 m, resulting in a reduction of lake volume by approximately 62 % and a concentration of remaining dissolved solutes in the residual waters. Consequently, under this phenomenon, the summer conductivity of this lake's water column, which is approximately 102 µS cm^{-1} (at its bottom), would theoretically increase to about 244 µS cm^{-1} during the ice-on period. This estimation reasonably corresponds with our below-ice measurement of 289 µS cm^{-1} obtained in April 2023.

The potential impact of solute cryoconcentration on water column conductivity can also be investigated in larger lakes where the effects of ionic segregation on their water conductivity during ice cover freezing should be less pronounced. FLL stands out as one of the largest lakes surveyed during the spring and summer seasons of 2023, benefiting from available bathymetric data. Bathymetry data derived from a three-dimensional model of FLL indicates a basin volume of 4.2 x 10^6 m^3 (Budkewitsch et al., 2011). With a surface area of 0.89 km^2, the formation of an approximately 1.7-meter-thick ice cover would theoretically reduce approximately 36 % of its water content, thereby leading to a proportional increase in conductivity by the same percentage. Therefore, with a mixed water column conductivity of approximately 111 µS cm^{-1} in the summer (site 12), we could anticipate the mean under-ice conductivity to shift to approximately 173 µS cm^{-1} due to solute cryoconcentration. This aligns with conductivity values measured in the stratified water column of site 12 (in April), which fall in the 141-173 µS cm^{-1} range below the saltier bottom waters having a conductivity 249 µS cm^{-1}.

The two previous simulations suggest that solute cryoconcentration may contribute (though its exact contribution remains unclear given our current lack of hydrochemical data) to the disparities observed between ice-on and ice-off water column conductivities in our surveyed lakes. However, it's crucial to acknowledge that this approach provides only a preliminary estimate of the under-ice mean water column conductivity due to ionic segregation during ice cover freezing. Confirming the accuracy of our model poses challenges due to the stratified nature of the water column in April. Further investigation and refinement of our methods are imperative to understand better and quantify the effects of solute cryoconcentration on water column conductivity. This includes acquiring hydrochemical data to enhance the accuracy of our estimates and considering additional factors that may influence conductivity variations between different seasonal periods. By conducting more comprehensive analyses, we can better understand the underlying processes driving conductivity dynamics in the surveyed lakes, including whether subpermafrost groundwater contributes to the observed conductivities.

CONCLUSION

Our study aimed to establish baseline data on water column temperature, conductivity, and occasionally pH for several lentic basins near the Rankin Inlet hamlet in the Kivalliq region of Nunavut. We utilized this dataset to infer variations in water column temperature and conductivity during ice-on and ice-off periods to understand the underlying causes. This newly acquired dataset supports the development of our thermal, geophysical, and conceptual coupled cryo-hydrogeological systems models used to simulate surface/subsurface hydrological flow within the continuous permafrost area. Specifically, we aim to develop novel robust techniques for identifying lakes potentially underlain by open taliks and to understand subsurface hydrogeological flow using an advanced cryo-hydrogeological model. In addition, our results will allow us to understand how climate change may affect lake water mixing dynamics in the future. In summary, based on our results, the following conclusions can be drawn:

1) A precise assessment of thermal unit depths (i.e., epilimnion, metalimnion, and hypolimnion) and their thicknesses within the water columns of our surveyed lakes is challenging due to discontinuities with depth in our physicochemical measurements. Moreover, measurements in the water column of many lakes often exist at only one depth, typically at the water/sediment interface, making it difficult to infer the thermal structure of the entire water column in such cases. Despite these challenges, our spring and late summer water column temperature measurements, supplemented by additional Agnico Eagle Meliadine Mine data in July 2011, strongly suggest that our targeted lakes can be categorized as cold continuous polymictic lakes. This classification suggests that they are thermally stratified only during the ice-on period, with deeper lakes exhibiting a more pronounced stratification.

2) Conductivity measurements in the lentic water bodies of interest provided an estimate of their TDS loading, falling well within the threshold for the upper threshold for freshwater (i.e., ~1000 ppm). Additionally, we observed an increase in conductivity with depth, with the highest values observed at or near the bottom, regardless of the sampling season. This phenomenon led us to infer a salinity-density relationship, possibly in conjunction with subpermafrost groundwater inflows, especially for the deepest sites within lakes suspected of hosting open taliks.

3) Our modelling suggests that solute cryoconcentration may contribute, to an extent that has yet to be determined, to the increase in water column conductivity during the ice-on period compared to the ice-off period. However, it's crucial to interpret these findings cautiously due to comparing values within a fully mixed water column (September) versus those in a stratified under-ice (April) environment. Further geochemical analyses are imperative to validate this hypothesis and ascertain whether this physical process primarily drives conductivity variations between ice-on and ice-off periods. These analyses should include measurements of major ion concentrations, along with additional bathymetric data for larger lakes such as LML and SLL. By conducting these analyses, we can gain a more comprehensive understanding of the underlying processes influencing conductivity dynamics, specifically related to TDS loading, in the studied water bodies.

ACKNOWLEDGEMENTS

This research project was funded by Natural Resources Canada's GEM-GeoNorth program. This research project benefited from the logistical support of the Iqalugaarjuup Nunanga Territorial Park. We thank the local Hunters & Trappers Organization, Kevin Brewer and Greg Oldenborger

from the GSC, for their field assistance. We also extend our gratitude to the internal reviewer for their constructive comments.

REFERENCES

Bell, T., & Brown, T. (2018). From science to policy in the eastern canadian arctic. An Integrated Regional Impact Study (IRIS) of climate change and modernization Synthesis and Recommendations. In *ArcticNet*.

Boehrer, B., & Schultze, M. (2008). Stratification of lakes. *Reviews of Geophysics*, *46*(2). https://doi.org/10.1029/2006RG000210

Boyce, F. M. (1974). Some Aspects of Great Lakes Physics of Importance to Biological and Chemical Processes. *Journal of the Fisheries Research Board of Canada*, *31*(5). https://doi.org/10.1139/f74-098

Brewer, M. C. (1958). The thermal regime of an Arctic lake. *Eos, Transactions American Geophysical Union*, *39*(2). https://doi.org/10.1029/TR039i002p00278

Budkewitsch, P., Prévost, C., Pavlic, G., & Pregitzer, M. (2011). *Description of water depth survey datasets from Rankin Inlet, Nunavut*. https://doi.org/https://doi.org/10.4095/288667

Dougherty, R. C. (2001). Density of salt solutions: Effect of ions on the apparent density of water. *Journal of Physical Chemistry B*, *105*(19). https://doi.org/10.1021/jp010097r

Dyke, A. S. (2004). An outline of North American deglaciation with emphasis on central and northern Canada. *Developments in Quaternary Science*, *2*(PART B). https://doi.org/10.1016/S1571-0866(04)80209-4

ECCC. (2023, October 1). *Historical climate data; Environment and Climate Change Canada*. <http://climate.weather.gc.ca/>.

Faucher, B., LeBlanc, A.-M., Utting, N., & Blade, M. (2022). *Assessment of physicochemical properties in lentic water bodies of the Rankin Inlet area (Nunavut) for sublacustrine open talik detection*. https://doi.org/10.4095/330212

Golder. (2012a). *SD 7-1 Aquatics Baseline Synthesis Report, 1994 to 2009 - Meliadine Gold Project, Nunavut – Meliadine Gold Project; unpublished report prepared by Golder Associates Ltd. for Agnico-Eagle Mines Limited, Doc 327-1013730076 Ver. 0.*

Golder. (2012b). *SD 7-2 2011. Aquatic Baseline Studies - Meliadine Gold Project, Nunavut – Meliadine Gold Project; unpublished report prepared by Golder Associates Ltd. for Agnico-Eagle Mines Limited, Doc 246-1013730076 Ver. 0. 77.*

Golder. (2014). *SD 6-1 permafrost thermal regime baseline studies – Meliadine Gold Project; unpublished report prepared by Golder Associates Ltd. for Agnico-Eagle Mines Limited, Doc 225-1314280007 Ver. 0.*

Golder. (2021). *Meliadine Extension – 2020 Thermal Assessment – Meliadine Gold Project; unpublished report prepared by Golder Associates Ltd. For Agnico-Eagle Mines Limited, Golder Doc 20136436-815-R-Rev2-2200*.

Goldman, C. R., Kumagai, M., & Robarts, R. D. (2012). Climatic Change and Global Warming of Inland Waters: Impacts and Mitigation for Ecosystems and Societies. In *Climatic Change and Global Warming of Inland Waters: Impacts and Mitigation for Ecosystems and Societies*. https://doi.org/10.1002/9781118470596

Killawee, J. A., Fairchild, I. J., Tison, J. L., Janssens, L., & Lorrain, R. (1998). Segregation of solutes and gases in experimental freezing of dilute solutions: Implications for natural glacial systems. *Geochimica et Cosmochimica Acta*, *62*(23–24). https://doi.org/10.1016/S0016-7037(98)00268-3

Kirillin, G., & Shatwell, T. (2016). Generalized scaling of seasonal thermal stratification in lakes. In *Earth-Science Reviews* (Vol. 161). https://doi.org/10.1016/j.earscirev.2016.08.008

Klanten, Y., Triglav, K., Marois, C., & Antoniades, D. (2021). Under-ice limnology of coastal valley lakes at the edge of the arctic ocean. *Arctic Science*, *7*(4). https://doi.org/10.1139/as-2020-0038

Lawley, C. J. M., McNicoll, V., Sandeman, H., Pehrsson, S., Simard, M., Castonguay, S., Mercier-Langevin, P., & Dubé, B. (2016). Age and geological setting of the Rankin Inlet greenstone belt and its relationship to the gold endowment of the Meliadine gold district, Nunavut, Canada. *Precambrian Research*, *275*. https://doi.org/10.1016/j.precamres.2016.01.008

LeBlanc, A.-M., Bellehumeur-Génier, O., Oldenborger, G. A., & Short, N. (2020). Lake area and shoreline changes due to climate and permafrost-related drivers, Rankin Inlet area, Nunavut. . In *Summary of Activities 2019, Canada-Nunavut Geoscience Office* (pp. 79–92).

LeBlanc, A.-M., Chartrand, J., & Smith, S. (2022). *Regional assessment of the occurrence of taliks below Arctic lakes. Geological Survey of Canada Scientific Presentation 138.* https://doi.org/https://doi.org/10.1139/as-2022-0002

LeBlanc, A.-M., & Oldenborger, G. A. (2021). Ground temperature, active-layer thickness and ground-ice conditions in the vicinity of Rankin Inlet, Nunavut. In *Summary of Activities 2020, Canada-Nunavut Geoscience Office* (pp. 63–72).

Lewis, W. M. (1983). A Revised Classification of Lakes Based on Mixing. *Canadian Journal of Fisheries and Aquatic Sciences*, *40*(10). https://doi.org/10.1139/f83-207

Mackay, J. R. (1963). *The Mackenzie Delta area, N.W.T. Department of Mines and Technical Surveys, Geographical Branch, Memoir 8.* https://doi.org/https://doi.org/10.4095/329313

Maloney, J. (2021). *From mineral exploration to advanced manufacturing: Developing value chains for critical minerals in Canada: Report of the Standing Committee on Natural Resources*. www.ourcommons.ca

McMartin, I. (2002). *Surficial geology, Rankin Inlet, Nunavut; Geological Survey of Canada, Open File 4116, scale 1:50 000.* https://doi.org/https://doi.org/10.4095/213219

McMartin, I., Gauthier, M. S., & Page, A. V. (2023). Updating the limits of the postglacial marine transgression along western Hudson Bay in Nunavut and Manitoba, Canada. *INQUA Congress 2023*.

Muster, S., Roth, K., Langer, M., Lange, S., Cresto Aleina, F., Bartsch, A., Morgenstern, A., Grosse, G., Jones, B., Sannel, A. B. K., Sjöberg, Y., Günther, F., Andresen, C., Veremeeva, A., Lindgren, R. P., Bouchard, F., Lara, J. M., Fortier, D., Charbonneau, S., … Boike, J. (2017). PeRL: A circum-Arctic Permafrost Region Pond and Lake database. *Earth System Science Data*, *9*(1). https://doi.org/10.5194/essd-9-317-2017

Oldenborger, G. A. (2024). *Time-domain electromagnetic soundings for talik investigations, Rankin Inlet, Nunavut; Geological Survey of Canada, Open File 9170, 118 p. https://doi.org/10.xxxx*.

Palmer, M. J., Chételat, J., Richardson, M., Jamieson, H. E., & Galloway, J. M. (2019). Seasonal variation of arsenic and antimony in surface waters of small subarctic lakes impacted by legacy mining pollution near Yellowknife, NT, Canada. *Science of the Total Environment*, *684*. https://doi.org/10.1016/j.scitotenv.2019.05.258

Randour, I., McMartin, I., & Roy, M. (2016). Study of the postglacial marine limit between Wager Bay and Chesterfield Inlet, western Hudson Bay, Nunavut. In *Canada-Nunavut Geoscience Office Summary of Activities* (pp. 51–60).

Santibáñez, P. A., Michaud, A. B., Vick-Majors, T. J., D'Andrilli, J., Chiuchiolo, A., Hand, K. P., & Priscu, J. C. (2019). Differential Incorporation of Bacteria, Organic Matter, and Inorganic Ions Into Lake Ice During Ice Formation. *Journal of Geophysical Research: Biogeosciences*, *124*(3). https://doi.org/10.1029/2018JG004825

Sladen, W. E., LeBlanc, A.-M., van der Sanden, J., & Chartrand, J. (2024, June). Using RADARSAT Constellation Mission Imagery to Support Talik Mapping, Rankin Inlet, Nunavut, Canada. *12th International Conference on Permafrost 2024*.

Taylor, M., Elliott, H. A., & Navitsky, L. O. (2018). Relationship between total dissolved solids and electrical conductivity in Marcellus hydraulic fracturing fluids. *Water Science and Technology*, *77*(8). https://doi.org/10.2166/wst.2018.092

van Everdingen, R. O. (1990). Ground-water hydrology. In T. D. Prowse & C. S. L. Ommanney (Eds.), *Northern hydrology: Canadian perspectives* (pp. 77–102). National Hydrology Research Institute, Environment Canada.

Yang, D., & Kane, D. L. (2020). Arctic hydrology, permafrost and ecosystems. In *Arctic Hydrology, Permafrost and Ecosystems*. https://doi.org/10.1007/978-3-030-50930-9

FIGURES

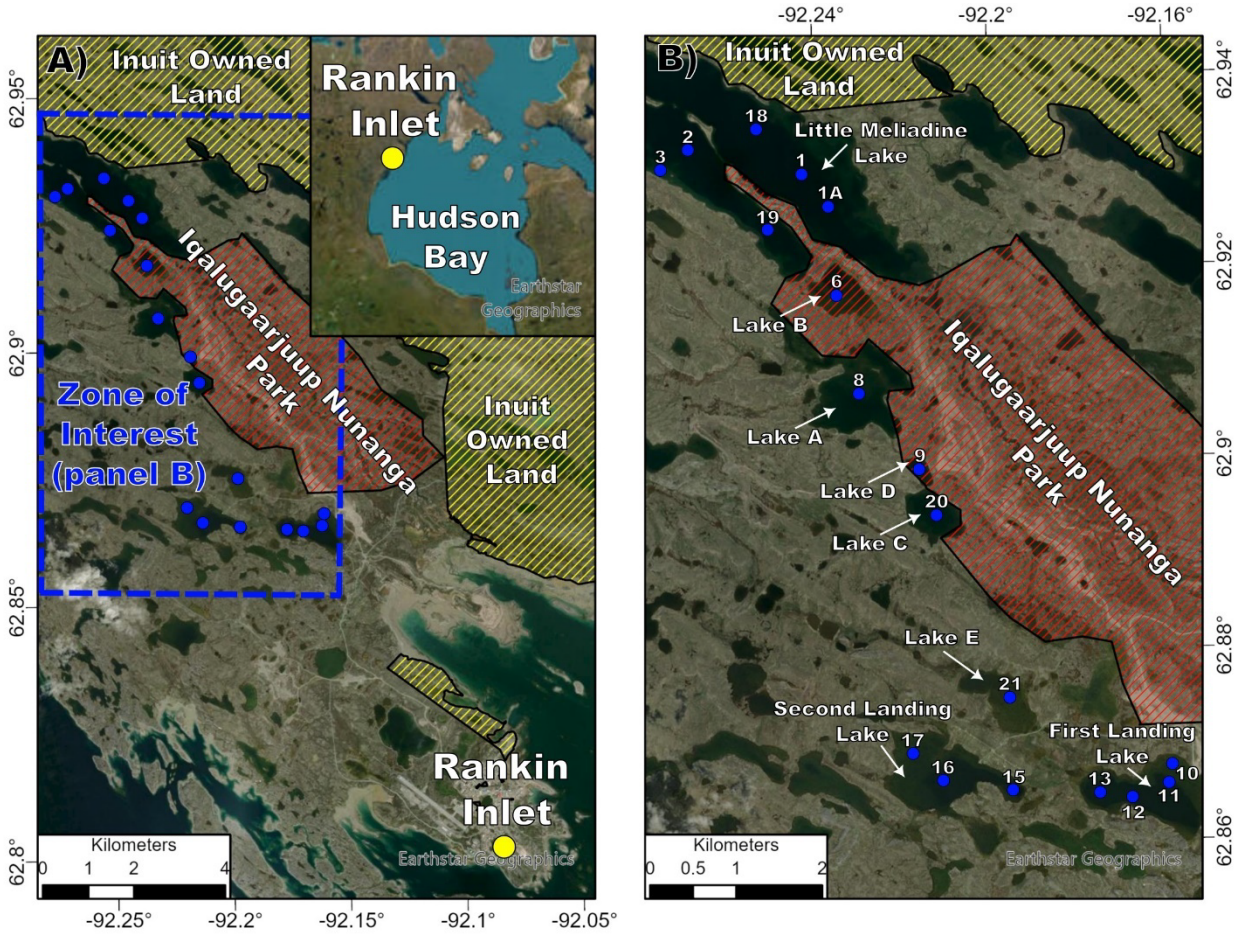

Figure 1: Location map of surveyed lentic basins and sites near Rankin Inlet (Nunavut, Canada) during the April and September 2023 field seasons. The positioning of the on-ice water column profile surveys (n=12; see Table A1) aligns with time-domain electromagnetic (TEM) soundings carried out in April 2023 for talik investigations (Oldenborger, 2024). September 2023 water column profiles (n=14; see Table A1) were conducted at some of the April 2023 TEM sites (excluding sites 1, 3, 8, 13 & 16) and additional ones (sites 1A, 10, 6, 9, 12A, 17, & 21).

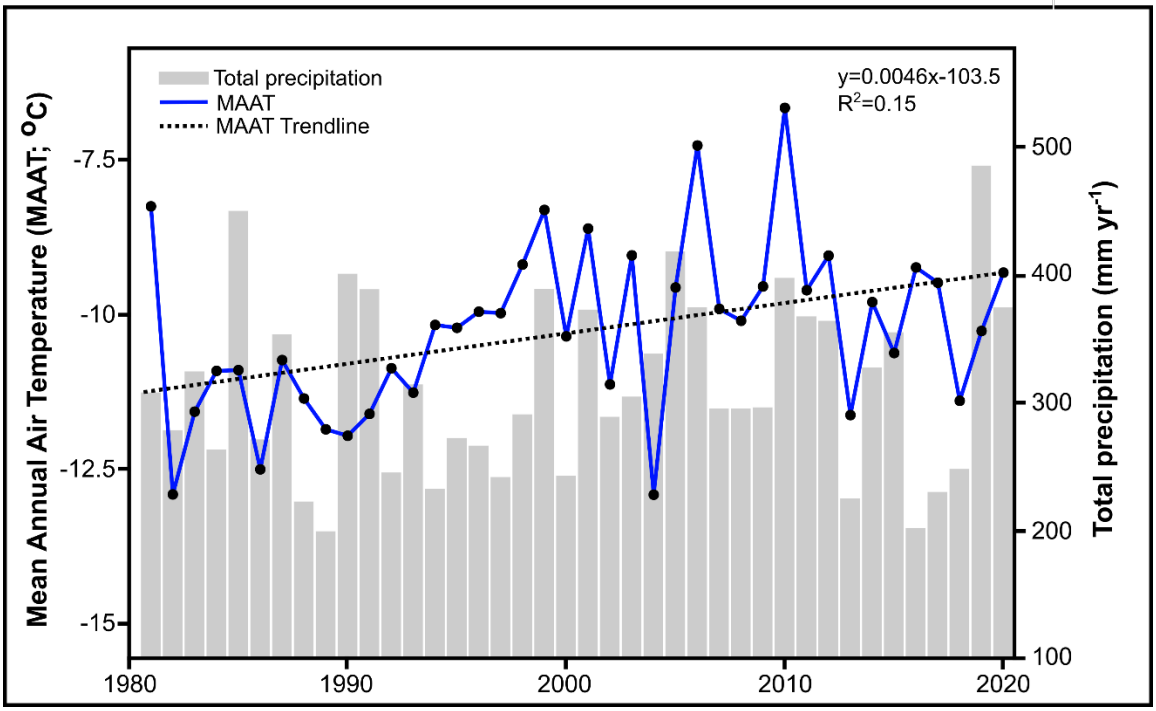

Figure 2: Time-series line and bar chart showing Rankin Inlet's Mean Annual Air Temperature (MAAT; °C) and total precipitation (mm yr^{-1}) during the 1981-2020 period. Data were taken from the Government of Canada's Historical Climate Data website (https://climate.weather.gc.ca/index_e.html). Figure from Faucher et al. (2022).

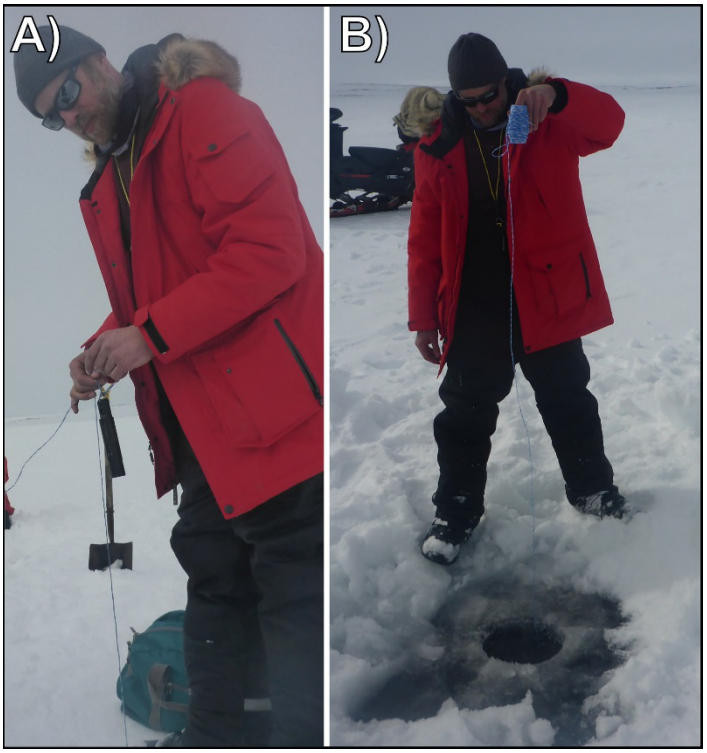

Figure 3: Setup for the on-ice depth profile surveys made on selected lentic basins near Rankin Inlet in April 2023. A) Installation of an Onset *HOBO U24* logger on a weighted line (photograph by K. Brewer; NRCan photo 2023-516); B) Logger slowly lowered down in one of the surveyed lakes via an ice cover hole (photograph by K. Brewer; NRCan photo 2023-517).

Figure 4: Photographs from the September 2023 field campaign showing A) a *DJI Matrice 300* RTK Unmanned Aerial Vehicle (UAV) used for the depth profile surveys (photograph by É. Girard; NRCan photo 2023-518); B) the *Solinst 5 LTC* and *HOBO MX2501* sondes attached to a 4mm thick Kevlar line attached to the UAV (photograph by É. Girard; NRCan photo 2023-519); and C) the UAV pilot flying the UAV during one of the lake physicochemical properties profile surveys (photograph by É. Girard; NRCan photo 2023-520).

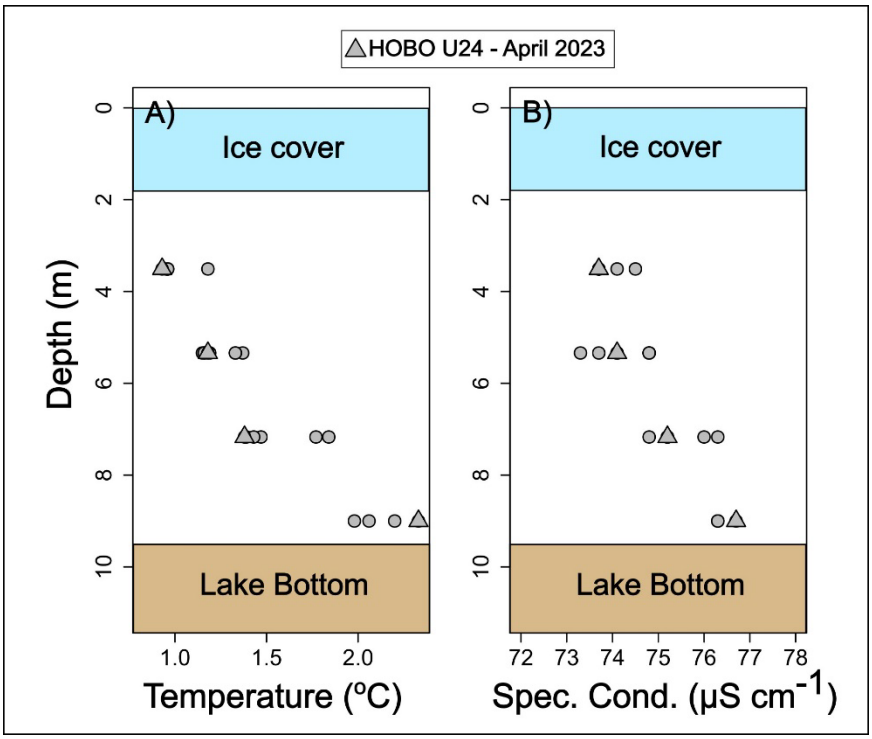

Figure 5: Temperature (A) and conductivity (Spec. Cond.; B) of the water column below the ~1.8 m thick ice cover at site 1 on Little Meliadine Lake in April 2023. Circles = non-water-unequilibrated values; Triangles = final (near-equilibrium) values.

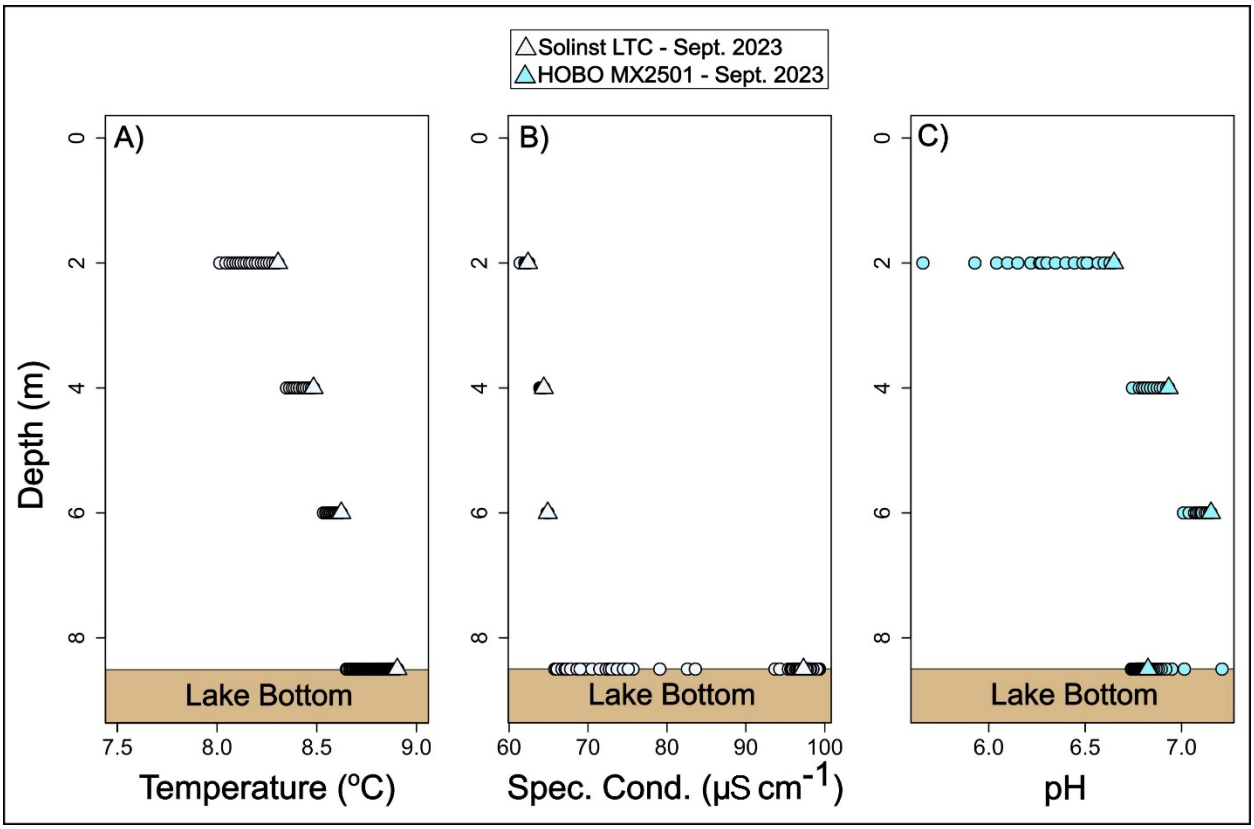

Figure 6: Temperature (A), conductivity (Spec. Cond.; B) and pH (C) of the water column at site 1A on Little Meliadine Lake in September 2023. Circles = non-water-unequilibrated values; Triangles = final (near-equilibrium) values.

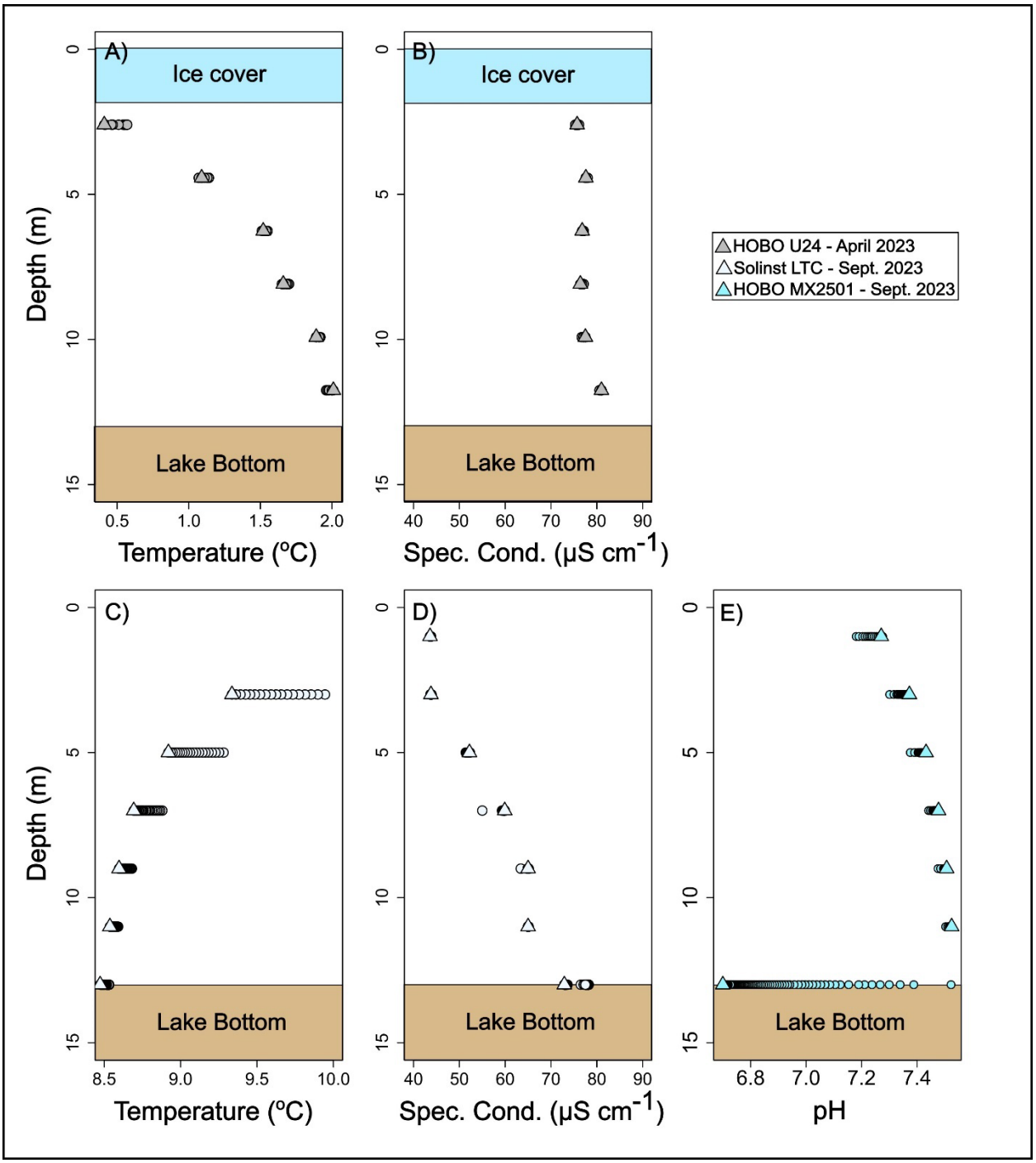

Figure 7: Temperature (A) and conductivity (Spec. Cond.; B) of the water column below the ~1.8 m thick ice cover at site 2 on Little Meliadine Lake in April 2023. Temperature (C), conductivity (Spec. Cond.; D) and pH (E) of the water column at the same location in September 2023. Circles = non-water-unequilibrated values; Triangles = final (near-equilibrium) values.

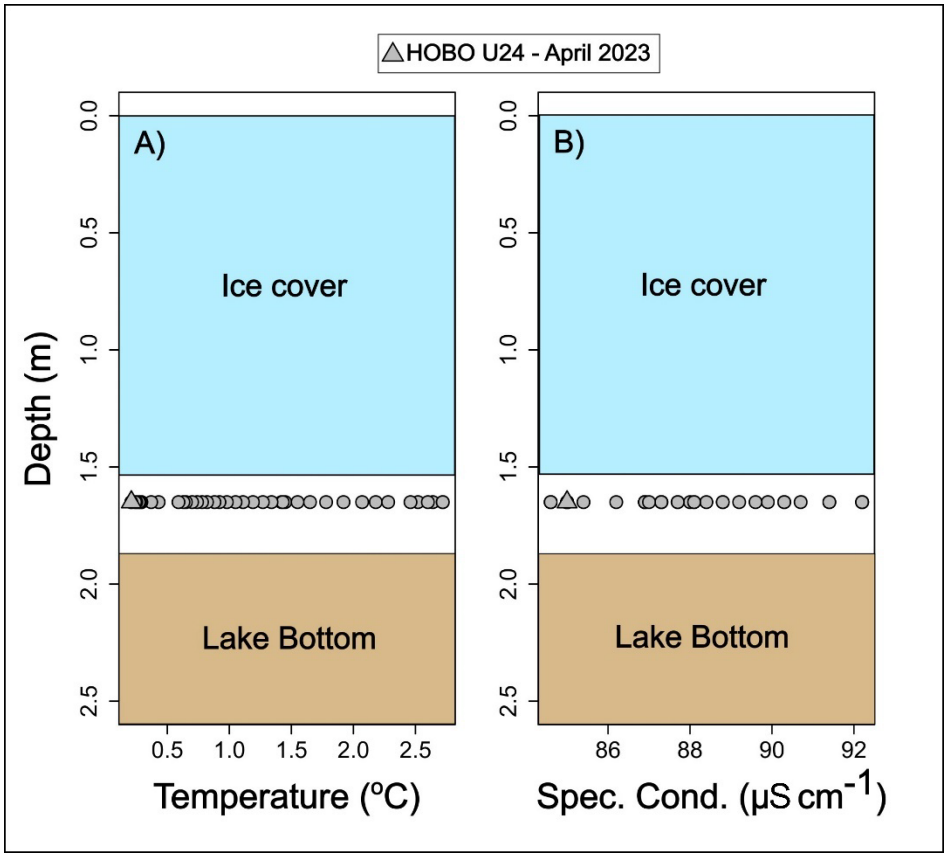

Figure 8: Temperature (A) and conductivity (Spec. Cond.; B) of the water column below the ~1.8 m thick ice cover at site 3 on Little Meliadine Lake in April 2023. Circles = non-water-unequilibrated values; Triangles = final (near-equilibrium) values.

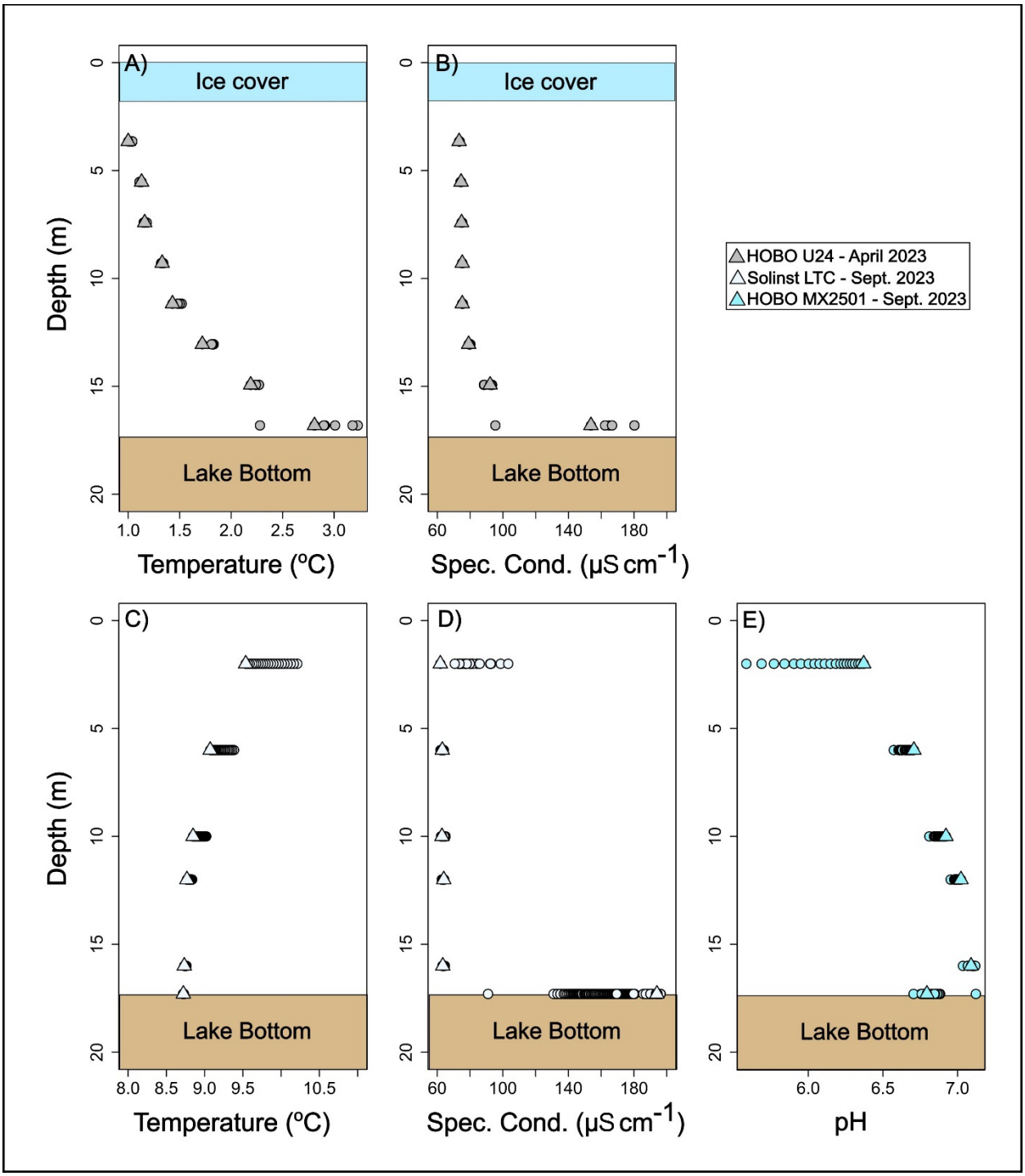

Figure 9: Temperature (A) and conductivity (Spec. Cond.; B) of the water column below the ~1.8 m thick ice cover at site 18 on Little Meliadine Lake in April 2023. Temperature (C), conductivity (Spec. Cond.; D) and pH (E) of the water column at the same location in September 2023. Circles = non-water-unequilibrated values; Triangles = final (near-equilibrium) values.

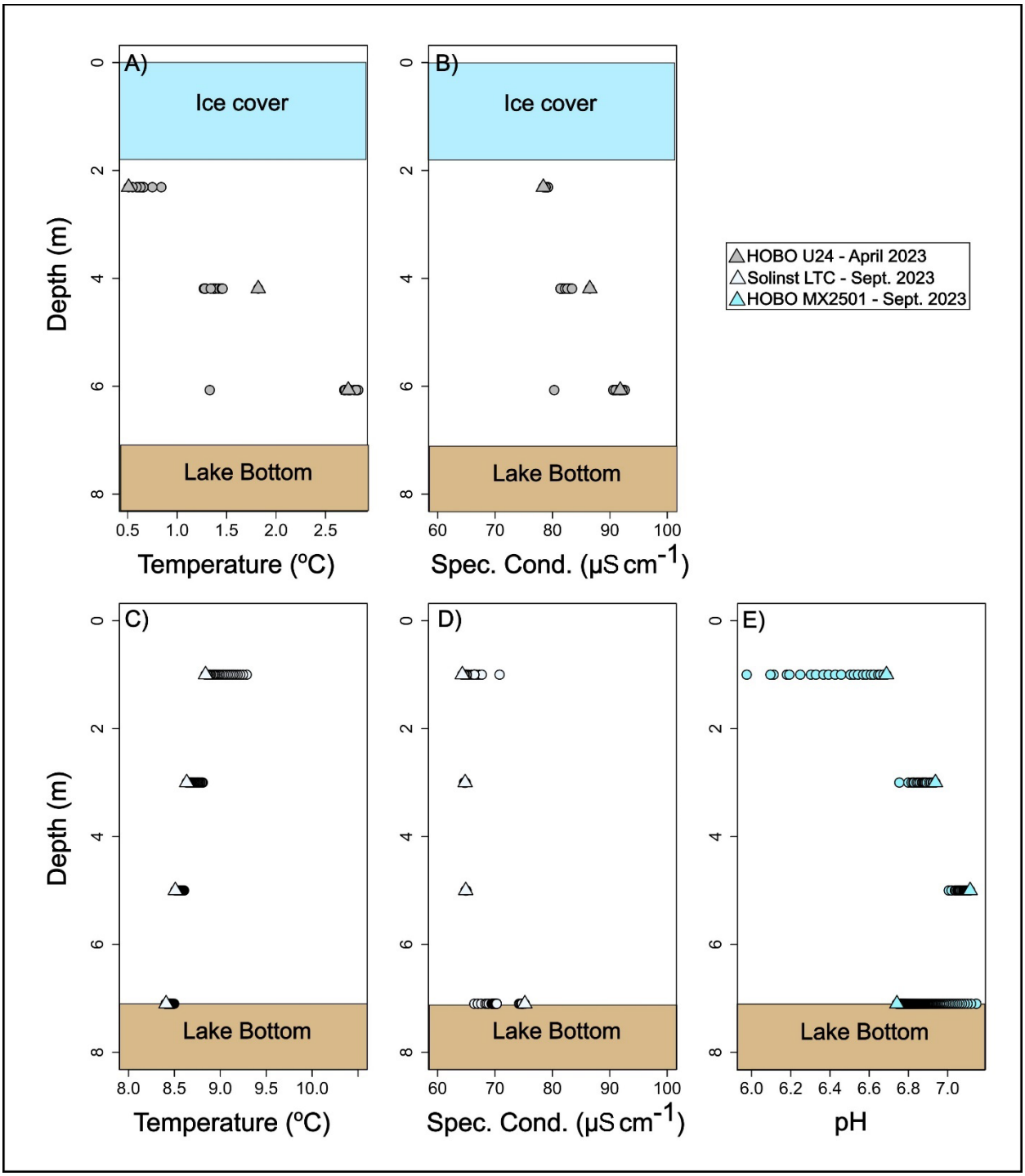

Figure 10: Temperature (A) and conductivity (Spec. Cond.; B) of the water column below the ~1.8 m thick ice cover at site 19 on Little Meliadine Lake in April 2023. Temperature (C), conductivity (Spec. Cond.; D) and pH (E) of the water column at the same location in September 2023. Circles = non-water-unequilibrated values; Triangles = final (near-equilibrium) values.

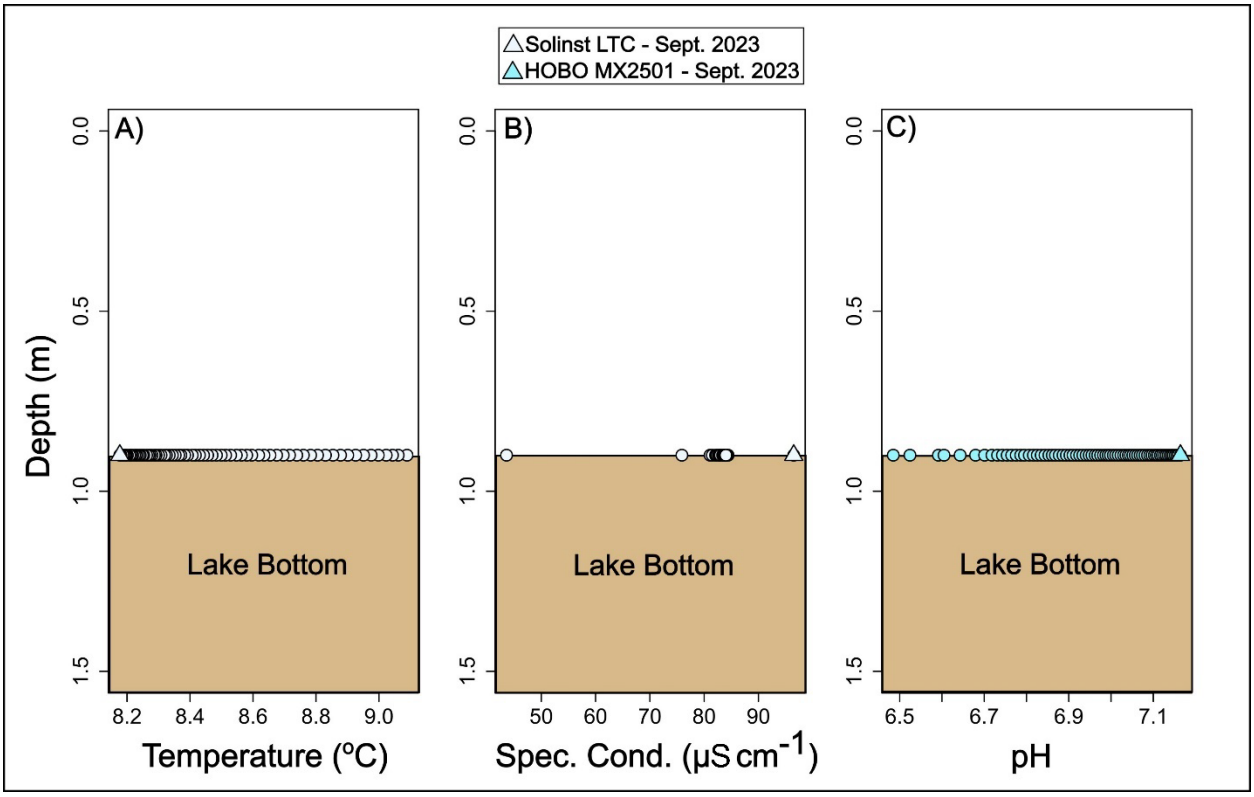

Figure 11: Temperature (A), conductivity (Spec. Cond.; B) and pH (C) of the bottom waters at site 10 on First Landing Lake in September 2023. Circles = non-water-unequilibrated values; Triangles = final (near-equilibrium) values.

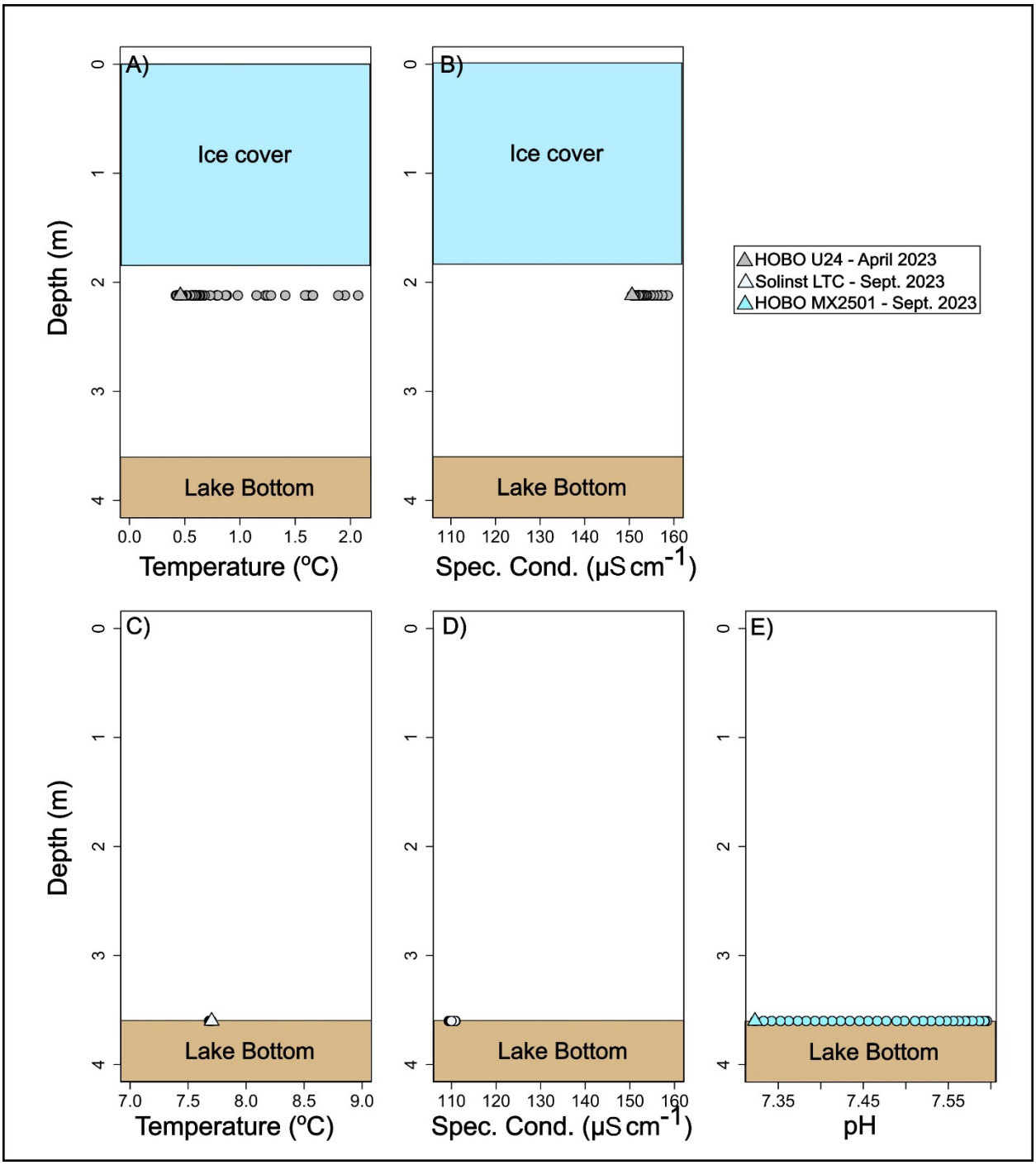

Figure 12: Temperature (A) and conductivity (Spec. Cond.; B) of the water column below the ~1.8 m thick ice cover at site 11 on First Landing Lake in April 2023. Temperature (C), conductivity (Spec. Cond.; D) and pH (E) of the bottom waters at the same location in September 2023. Circles = non-water-unequilibrated values; Triangles = final (near-equilibrium) values.

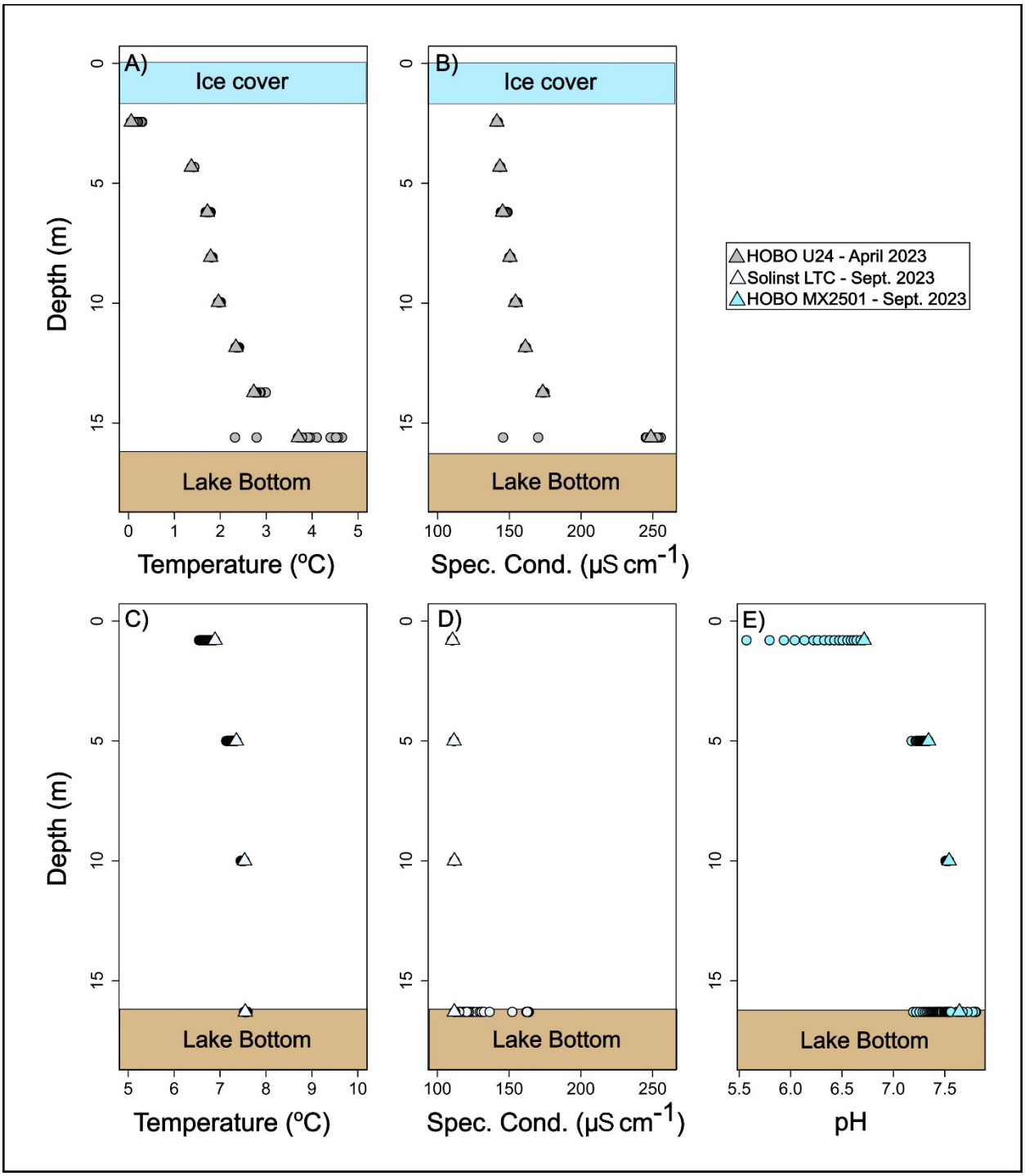

Figure 13: Temperature (A) and conductivity (Spec. Cond.; B) of the water column below the ~1.8 m thick ice cover at site 12 on First Landing Lake in April 2023. Temperature (C), conductivity (Spec. Cond.; D) and pH (E) of the water column at the same location in September 2023. Circles = non-water-unequilibrated values; Triangles = final (near-equilibrium) values.

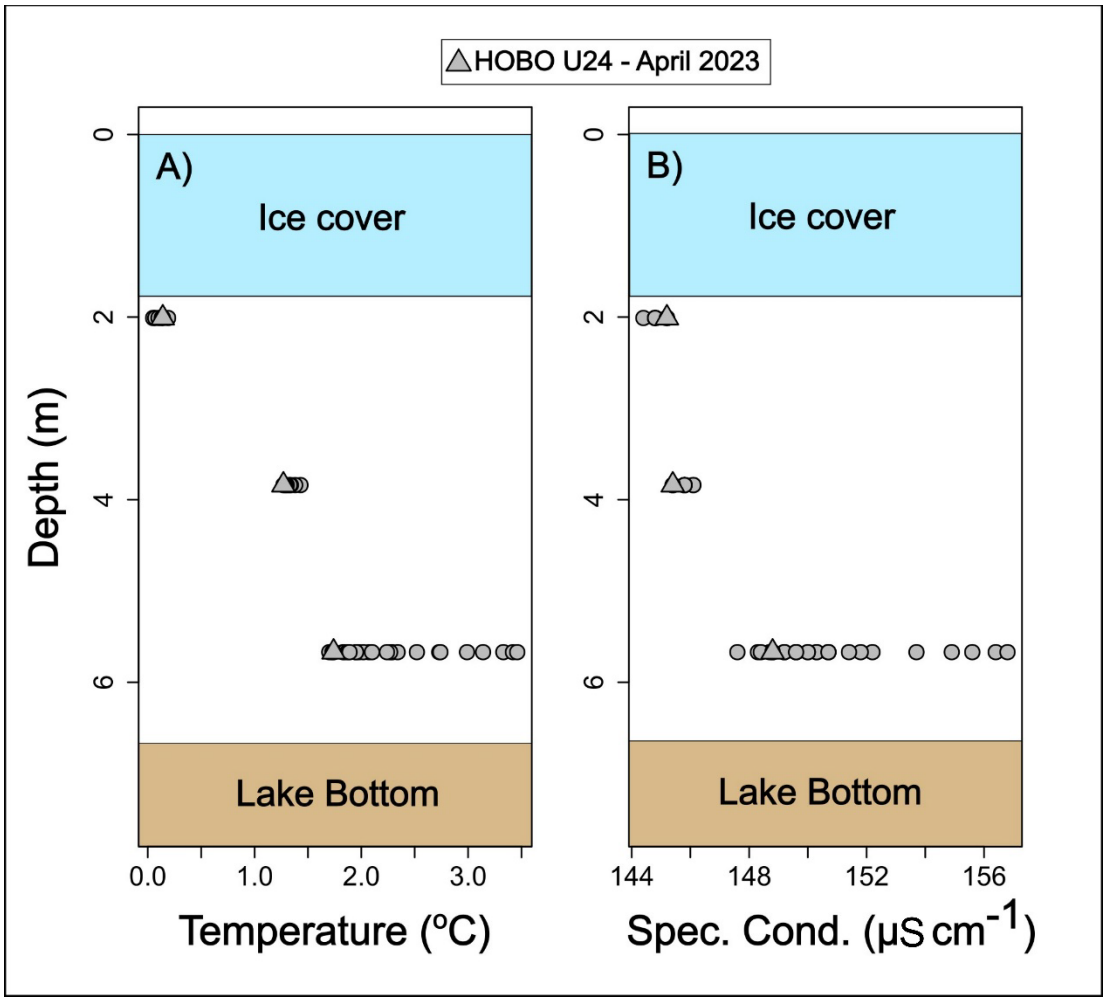

Figure 14: Temperature (A) and conductivity (Spec. Cond.; B) of the water column below the ~1.8 m thick ice cover at site 13 on First Landing Lake in April 2023. Circles = non-water-unequilibrated values; Triangles = final (near-equilibrium) values.

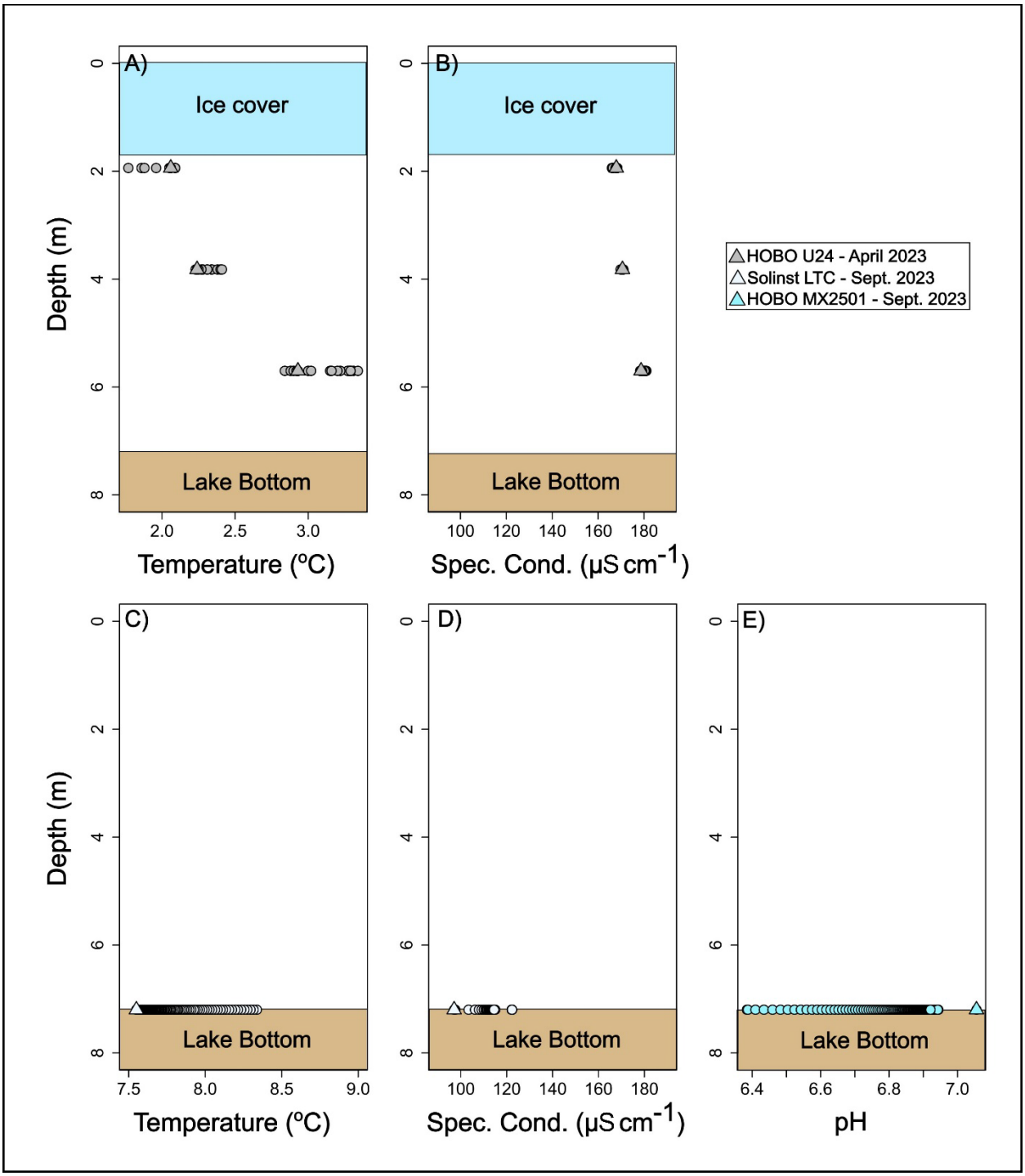

Figure 15: Temperature (A) and conductivity (Spec. Cond.; B) of the water column below the ~1.8 m thick ice cover at site 15 on Second Landing Lake in April 2023. Temperature (C), conductivity (Spec. Cond.; D) and pH (E) of the bottom waters at the same location in September 2023. Circles = non-water-unequilibrated values; Triangles = final (near-equilibrium) values.

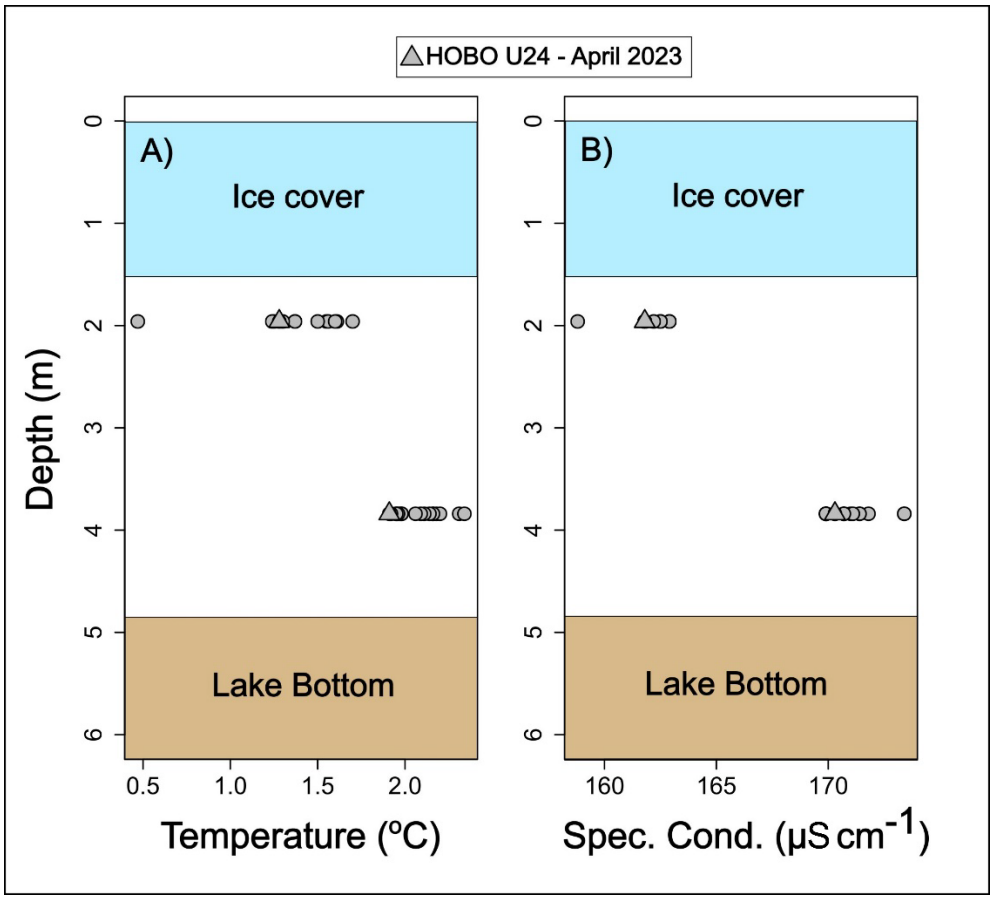

Figure 16: Temperature (A) and conductivity (Spec. Cond.; B) of the water column below the ~1.8 m thick ice cover at site 16 on Second Landing Lake in April 2023. Circles = non-water-unequilibrated values; Triangles = final (near-equilibrium) values.

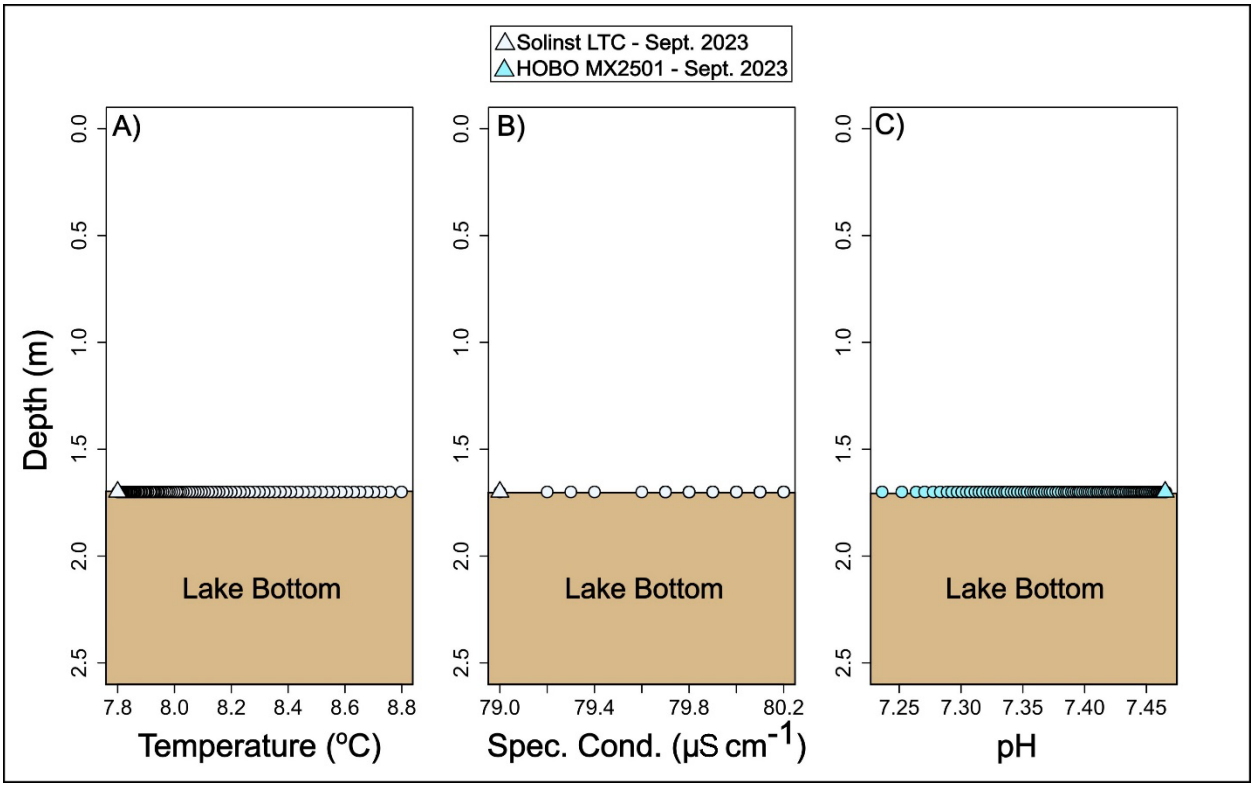

Figure 17: Temperature (A), conductivity (Spec. Cond.; B) and pH (C) of the water column at site 17 on Second Landing Lake in September 2023. Circles = non-water-unequilibrated values; Triangles = final (near-equilibrium) values.

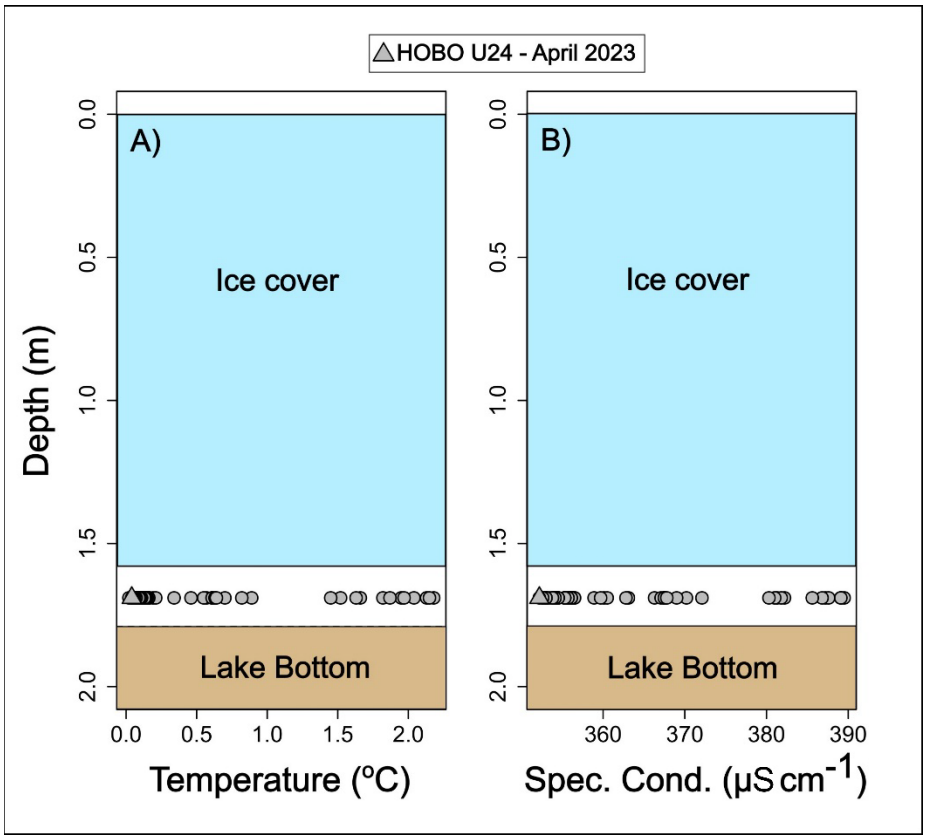

Figure 18: Temperature (A) and conductivity (Spec. Cond.; B) of the near-bottom waters below the ~1.6 m thick ice cover at site 8 on Lake A in April 2023. Circles = non-water-unequilibrated values; Triangles = final (near-equilibrium) values.

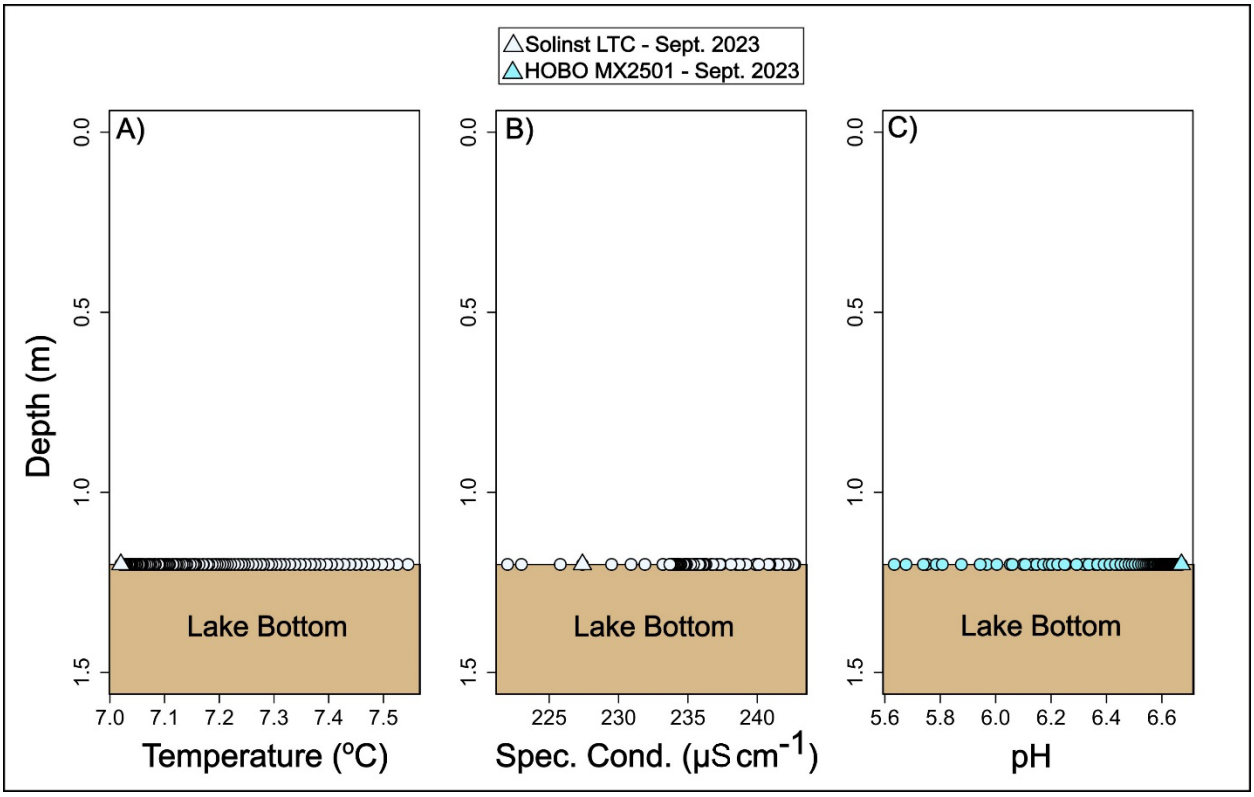

Figure 19: Temperature (A), conductivity (Spec. Cond.; B) and pH (C) of the bottom waters at site 6 on Lake B in September 2023. Circles = non-water-unequilibrated values; Triangles = final (near-equilibrium) values.

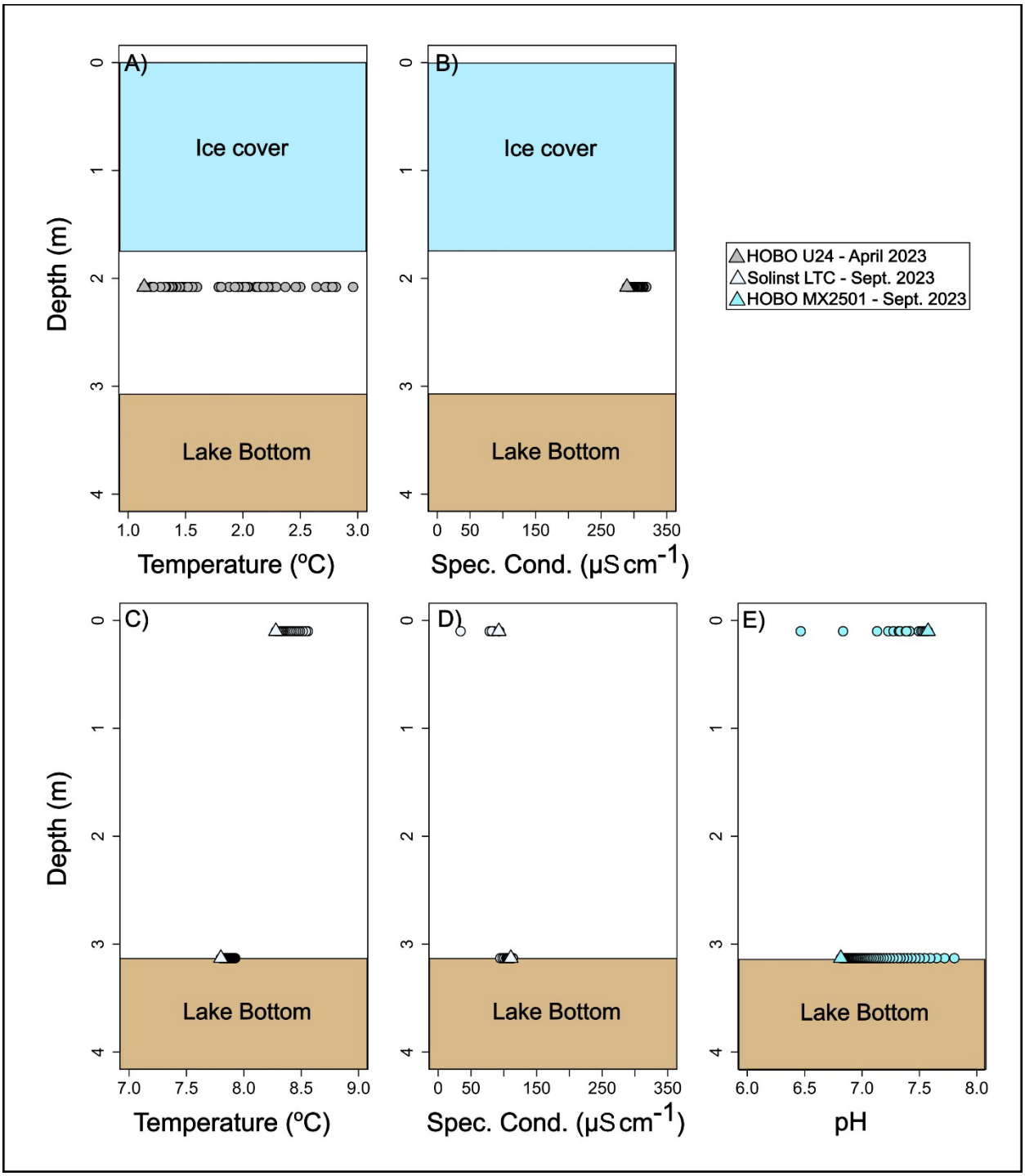

Figure 20: Temperature (A) and conductivity (Spec. Cond.; B) of the water column below the ~1.8 m thick ice cover at site 20 on Lake C in April 2023. Temperature (C), conductivity (Spec. Cond.; D) and pH (E) of the upper and bottom waters at the same location in September 2023. Circles = non-water-unequilibrated values; Triangles = final (near-equilibrium) values.

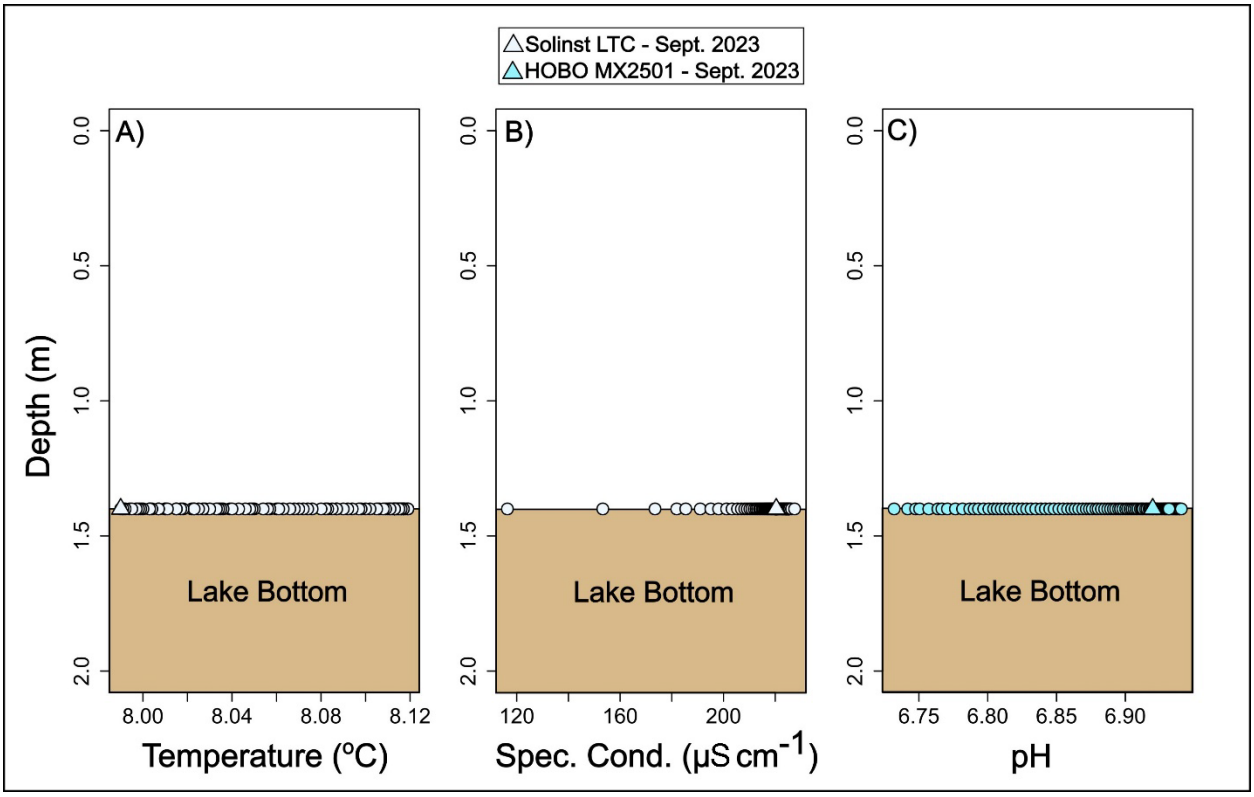

Figure 21: Temperature (A), conductivity (Spec. Cond.; B) and pH (C) of the bottom waters at site 9 on Lake D in September 2023. Circles = non-water-unequilibrated values; Triangles = final (near-equilibrium) values.

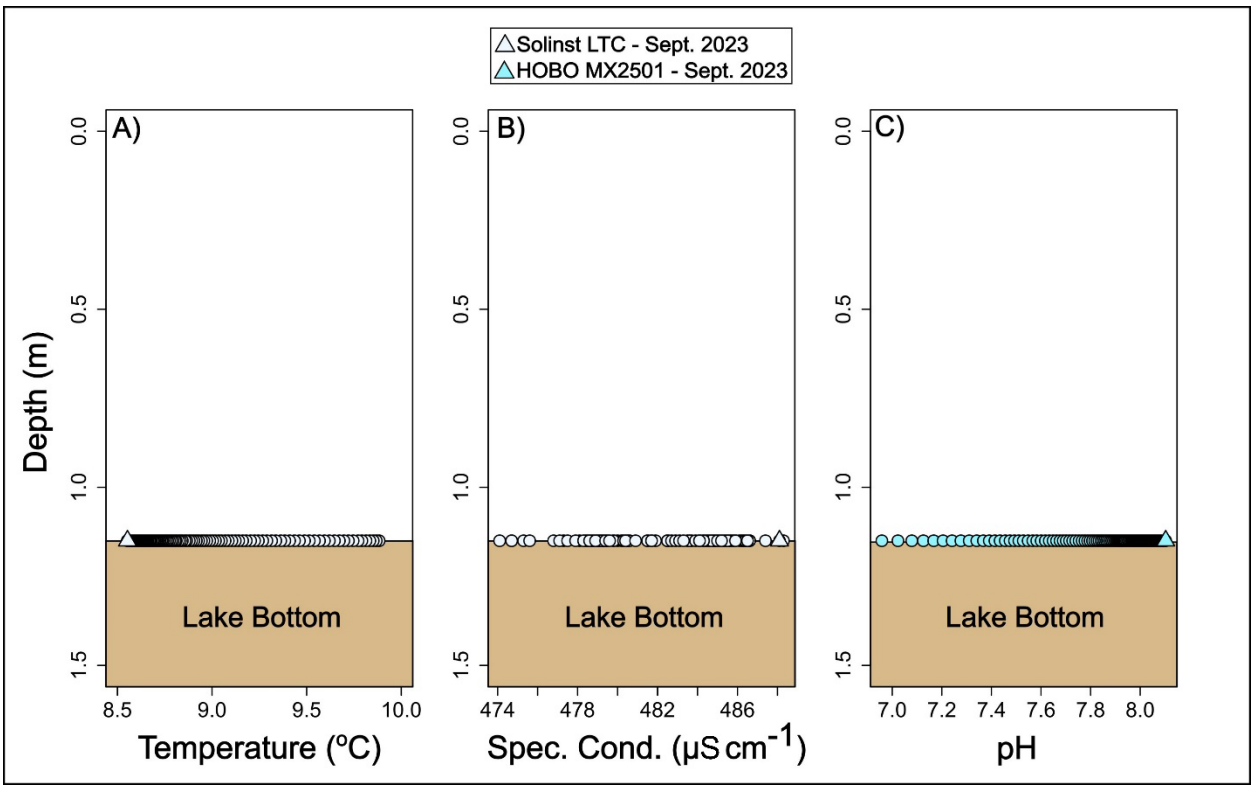

Figure 22: Temperature (A), conductivity (Spec. Cond.; B) and pH (C) of the bottom waters at site 21 on Lake E in September 2023. Circles = non-water-unequilibrated values; Triangles = final (near-equilibrium) values.

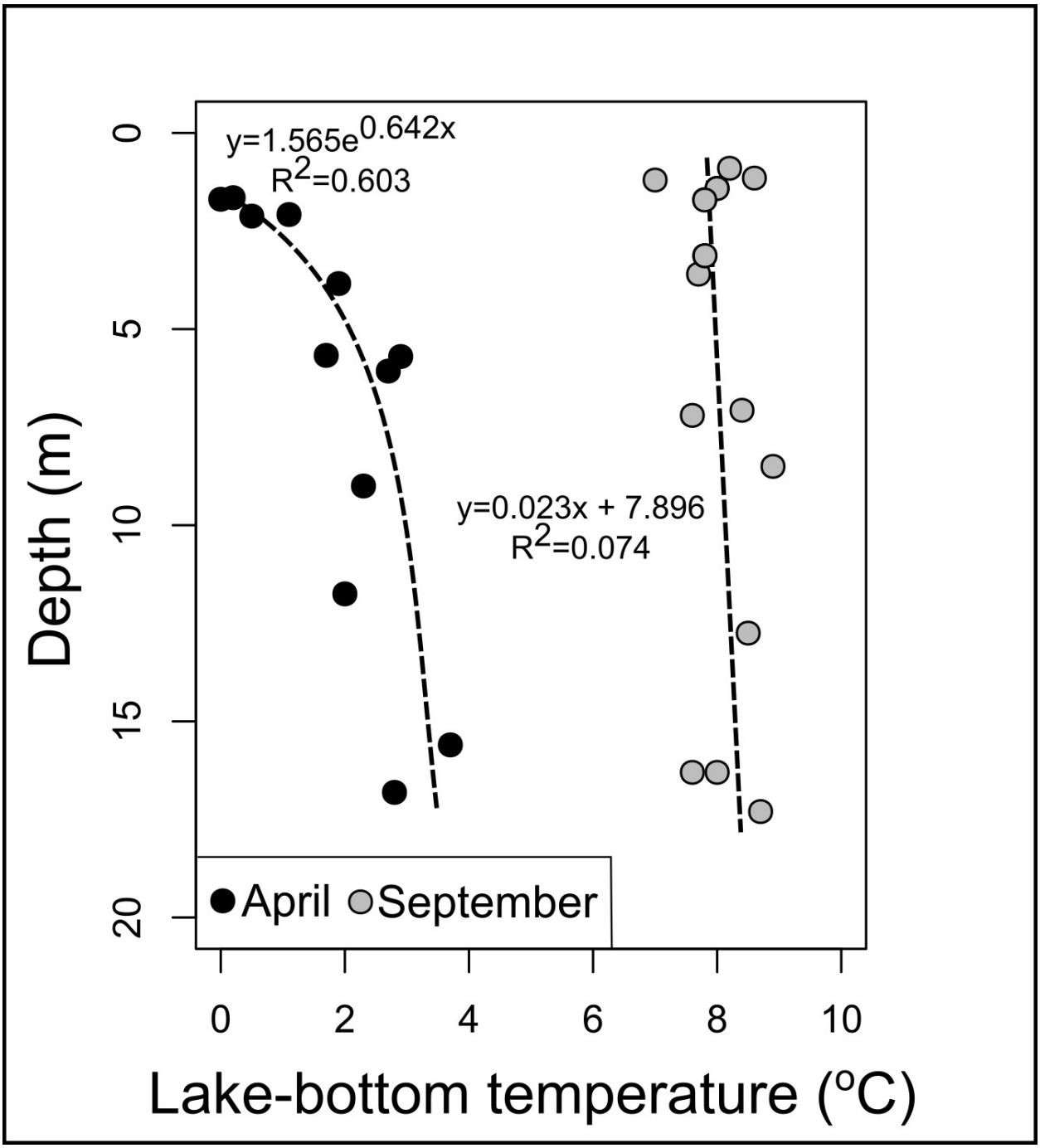

Figure 23: Lake-bottom temperature at surveyed sites during the ice-on (April; black dots) and ice-off (September; gray dots) periods in 2023. Note that the water temperature readings from shallow water beneath the ice in April might be slightly higher than shown here. This could be because of cooling caused by the shallow water's contact with the cold air during our surveys. Additionally, the low volume of water at those sites may have contributed to this cooling effect.

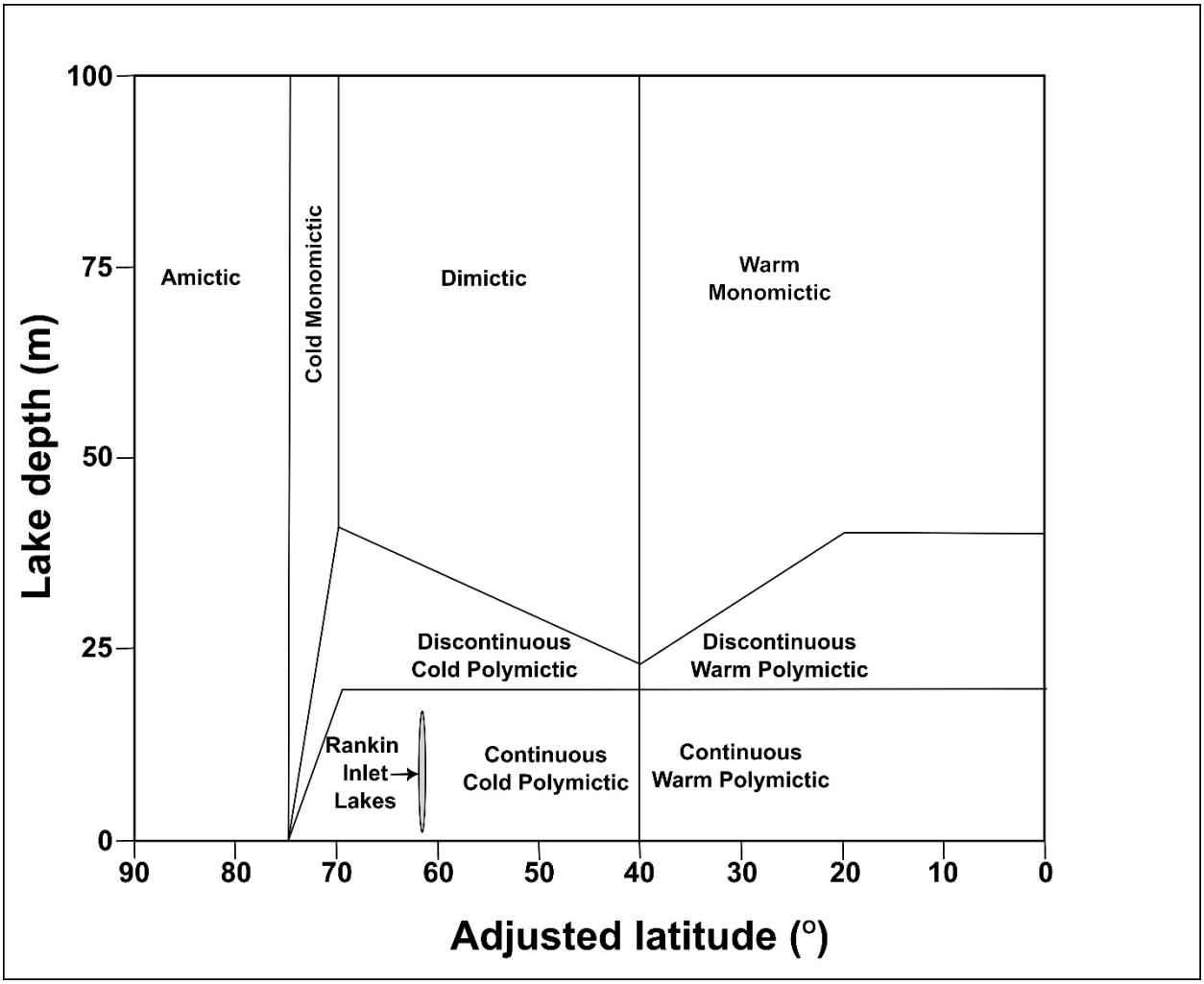

Figure 24: Estimated distribution of lake types according to their adjusted latitude and depth (based on Fig. 2 in Lewis, 1983). Lakes of interest within the Rankin Inlet area (grey ellipse) are situated at a latitude of ~62.8°N and have shallow depths (<20 m); those should fall under the Continuous Cold Polymictic category.

APPENDIX

Table A1: Summary table of physicochemical attributes (temperature, conductivity, and pH) within the water column of surveyed sites (according to the lakes in which they were conducted) during the spring (April) and late summer (September) 2023 field campaigns. Physicochemical attribute values presented here are the final recorded ones at various surveyed depths (i.e., at the end of our 3-minute and 30-second steps for April and September surveys, respectively). Total dissolved solids (TDS) loading was approximated by multiplying the conductivity values (in µS cm^{-1}) of our freshwater basins by 0.7 (e.g., Taylor et al., 2018).

Sampling site	Latitude (°N)	Longitude (°E)	Surface area (km^2)	Basin's maximum depth (m)	Surveyed site's maximum depth (m)	Survey dates	Depth (m)	Temperature (°C)	Conductivity (µS cm^{-1})	pH	Approximated TDS (ppm)
Little Meliadine Lake			***5.27***	***NA (≥17.3)***							
Site 1	62.9297	-92.2426			9.42	2023-04-27	3.51	0.9	74	NA	51.8
						"	5.34	1.2	74	NA	51.8
						"	7.17	1.4	75	NA	52.5
						"	9.00	2.3	77	NA	53.9
Site 1A	62.9263	-92.2366			8.50	2023-09-08	2.00	8.3	62	6.7	43.4
						"	4.00	8.5	64	6.9	44.8
						"	6.00	8.6	65	7.2	45.5
						"	8.50	8.9	97	6.8	67.9
Site 2	62.9323	-92.2686			12.75	2023-04-27	2.60	0.4	76	NA	53.2
						"	4.43	1.1	78	NA	54.6
						"	6.26	1.5	77	NA	53.9
						"	8.09	1.7	76	NA	53.2
						"	9.92	1.9	78	NA	54.6
						"	11.75	2.0	81	NA	56.7
						2023-09-09	1.00	10.1	44	7.3	30.8
						"	3.00	9.3	44	7.4	30.8
						"	5.00	8.9	52	7.4	36.4
						"	7.00	8.7	60	7.5	42
						"	9.00	8.6	65	7.5	45.5
						"	11.00	8.5	65	7.5	45.5
						"	12.75	8.5	73	6.7	51.1
Site 3	62.9302	-92.2749			1.87	2023-04-27	1.65	0.2	85	NA	59.5
Site 18	62.9344	-92.2528			17.26	2023-04-27	3.65	1.0	73	NA	51.1
						"	5.53	1.1	75	NA	52.5
						"	7.41	1.2	75	NA	52.5
						"	9.29	1.3	75	NA	52.5
						"	11.17	1.4	75	NA	52.5
						"	13.05	1.7	79	NA	55.3
						"	14.93	2.2	92	NA	64.4
						"	16.81	2.8	154	NA	107.8
						2023-09-09	2.00	9.5	62	6.4	43.4
						"	6.00	9.1	63	6.7	44.1
						"	10.00	8.9	63	6.9	44.1
						"	12.00	8.8	64	7	44.8
						"	16.00	8.7	63	7.1	44.1

						"	17.30	8.7	194	6.8	135.8
Site 19	62.9239	-92.2505			7.07	2023-04-27	2.31	0.5	78	NA	54.6
						"	4.19	1.8	87	NA	60.9
						"	6.07	2.7	92	NA	64.4
						2023-09-09	1.00	8.8	64	6.7	44.8
						"	3.00	8.6	65	6.9	45.5
						"	5.00	8.5	65	7.1	45.5
						"	7.07	8.4	75	6.7	52.5
First Landing Lake			***0.89***	***17.6[1]***							
Site 10	62.8678	-92.1595			0.90	2023-09-11	0.90	8.2	97	7.2	67.9
Site 11	62.8659	-92.1603			3.60	2023-04-27	2.12	0.5	151	NA	105.7
						2023-09-06	3.60	7.7	110	7.3	77
Site 12	62.8644	-92.1687			16.60	2023-04-28	2.44	0.1	141	NA	98.7
						"	4.32	1.4	143	NA	100.1
						"	6.20	1.7	145	NA	101.5
						"	8.08	1.8	150	NA	105
						"	9.96	2.0	154	NA	107.8
						"	11.84	2.3	161	NA	112.7
						"	13.72	2.7	173	NA	121.1
						"	15.60	3.7	249	NA	174.3
						2023-09-06	0.80	6.9	111	6.7	77.7
						"	5.00	7.4	112	7.3	78.4
						"	10.00	7.5	112	7.5	78.4
						"	16.30	7.6	112	7.6	78.4
Site 13	62.8649	-92.1759			6.67	2023-04-28	2.01	0.1	145	NA	101.5
						"	3.84	1.3	145	NA	101.5
						"	5.67	1.7	149	NA	104.3
Second Landing Lake			***0.94***	***NA (≥7.20)***							
Site 15	62.8653	-92.1961			7.20	2023-04-28	1.94	2.1	168	NA	117.6
						"	3.82	2.2	171	NA	119.7
						"	5.70	2.9	179	NA	125.3
						2023-09-10	7.20	7.6	97	7.1	67.9
Site 16	62.8663	-92.2119			4.84	2023-04-28	1.96	1.3	162	NA	113.4
						"	3.84	1.9	170	NA	119
Site 17	62.8692	-92.2187			1.70	2023-09-10	1.70	7.8	79	7.5	55.3
Lake A			***0.99***	***NA (≥1.79)***							
Site 8	62.9067	-92.2301			1.79	2023-04-28	1.69	0.1	352	NA	246.4
Lake B			***0.31***	***NA (≥1.20)***							
Site 6	62.917	-92.2349			1.20	2023-09-08	1.20	7.0	227	6.7	158.9
Lake C			***0.30***	***NA (≥3.13)***							
Site 20	62.8939	-92.2127			3.13	2023-04-28	2.08	1.1	289	NA	202.3
						2023-09-10	0.10	8.3	93	7.6	65.1
						"	3.13	7.8	111	6.8	77.7
Lake D			***0.06***	***NA (≥1.40)***							
Site 9	62.8988	-92.2165			1.40	2023-09-10	1.41	8.0	220	6.9	154
Lake E			***0.36***	***NA (≥1.15)***							
Site 21	62.8749	-92.1964			1.15	2023-09-10	1.15	8.6	488	8.1	341.6

[1]Based on Budkewitsch et al. (2011)

Table A2: July and August 2011 water column temperatures (top, bottom, and differences between both) for lakes situated in the periphery of the Agnico Eagle Meliadine Mine (data from Golder, 2012).

Lake/Sampling Site	Latitude (°N)	Longitude (°E)	Surface area (km^2)	Maximum basin depth (m)	Survey date	Top T (°C)	Bottom T (°C)	ΔT (°C)
B2	63.0070	-92.2620	0.49	3.60	7/20/2011	14.2	14.2	0
B45	62.9990	-92.2270	0.48	2.40	7/21/2011	15.2	15.2	0
B46	62.9980	-92.2060	0.45	2.10	7/24/2011	19.1	19.1	0
D4	63.0310	-92.3120	0.17	1.60	7/17/2011	14.6	14.6	0
D5	63.0320	-92.3010	0.06	2.40	7/17/2011	17.1	17.1	0
D7	63.0280	-92.2770	0.69	2.80	7/22/2011	15.2	14.9	0.3
D23	63.0340	-92.2960	0.14	3.00	7/18/2011	14.3	14.3	0
E3	63.0470	-92.2860	0.54	4.60	7/19/2011	14.3	14.2	0.1
E4	63.0370	-92.2730	0.08	3.90	7/19/2011	14.5	14.0	0.5
Meliadine - E	63.0175	-92.1342	126.00	7.80	8/1/2011	14.9	14.7	0.2
Meliadine - SE	63.0056	-92.2889	126.00	4.50	7/27/2011	17.8	17.7	0.1
Booth-2	63.0281	-92.1608	126.00	10.00	7/31/2011	15.0	14.6	0.4
Control	63.0090	-92.3190	1.25.00	5.60	7/29/2011	16.8	16.7	0.1